

Dynamical structures of misaligned circumbinary planets under hierarchical three-body systems

Hanlun Lei^{1,2*}, Yan-Xiang Gong^{3†}

¹*School of Astronomy and Space Science, Nanjing University, Nanjing 210023, China*

²*Key Laboratory of Modern Astronomy and Astrophysics in Ministry of Education, Nanjing University, Nanjing 210023, China*

³*College of Physics and Electronic Engineering, Taishan University, Taian 271000, China*

Accepted. Received; in original form

ABSTRACT

All circumbinary planets (CBPs) currently detected are located in almost co-planar configurations with respect to the binary orbit, due to the fact that CBPs with higher misalignment are more difficult to detect. However, observations of polar circumbinary gas and debris disks in recent years and long-term orbital stability of inclined planets indicate that it is possible to form misaligned CBPs around eccentricity binaries (even polar CBPs). In this work we focus on the dynamical structures of CBPs in a wide range of parameters in order to provide a guidance for the space where the binary can host planets for a long enough time. To this end, the dynamical model is approximated as a hierarchical three-body problem, and the secular approximation is formulated up to the hexadecapolar order in semimajor axis ratio. Dynamical maps show that there are complex structures in the parameter space. A web of secular resonances is produced in the entire parameter space and it can well explain those numerical structures arising in dynamical maps. Based on perturbative treatments, an adiabatic invariant is introduced and thus dynamical structures can be explored by analysing phase portraits. It is found that (a) the quadrupole-order resonance (nodal resonance) is responsible for the distribution of V-shape region, and high-order and secondary resonances dominate those structures inside or outside V-shape region, and (b) the secondary 1:1 resonance is the culprit causing symmetry breaking of dynamical structures inside polar region.

Key words: celestial mechanics – planets and satellites: dynamical evolution and stability – planetary systems

1 INTRODUCTION

Stellar binaries or multiples are popular in the Universe and, for massive stars, the fraction can reach up to 70% (Tokovinin 1997). There are about a hundred of planets detected in multiple-star systems (Martin 2018). In particular, planets in binary systems may be located in either circumstellar (S-type) or circumbinary (P-type) configurations. A dominant fraction of planets in binary systems are found in the S-type configurations. There is about more than a dozen of circumbinary planets (CBPs) in the P-type configurations observed by the Kepler and TESS space telescopes (Georgakarakos et al. 2024; Kostov et al. 2020, 2016, 2021). The lack of P-type planets may be ascribed to observational biases and dynamical processes (Cuello & Giuppone 2019). All the CBPs currently detected are located in almost co-planar

configurations with respect to the binary orbit, which is a consequence of observational bias instead of a representative of the underlying population (Czekala et al. 2019).

In recent years, misaligned gas or debris disks have been observed around stellar binaries, such as 99 Herculis (Kennedy et al. 2012), IRS 43 (Brinch et al. 2016), GG Tau (Cazzoletti et al. 2017), HD 142527 (Verhoeff et al. 2011), HD 98800 B (Kennedy et al. 2012) and AC Her (Martin et al. 2023), suggesting that misaligned planet formation is possible. As for the stability of P-type planets, polar orbits are stable over a wide range of binary parameters (Chen et al. 2020; Cuello & Giuppone 2019). Based on N -body simulations, it is shown that terrestrial planet formation around an eccentric binary is more likely in a polar configuration than in a coplanar configuration (Childs & Martin 2021). Martin & Lubow (2017) showed that misaligned discs should be more common around long-period and eccentric stellar binaries. Therefore, misaligned (even polar) orbits provide appropriate dynamical environments for planet formation. The

* leihl@nju.edu.cn

† yxgong@tsu.edu.cn

reason why there are no highly misaligned or polar CBPs detected so far is that misaligned CBPs are usually difficult to detect due to long orbital periods as well as complex spectra of stellar binaries (Martin & Triaud 2014).

Misaligned terrestrial CBPs could form in the presence of a misaligned circumbinary gas disk, which can help to nodally align planetary orbits and maintain planetary inclination during the formation process (Childs & Martin 2022). As the first observational evidence of a polar circumbinary planet, the post-AGB star binary system (AC Her) is found to hold a dust disk where the inner edge is much farther out than the tidal truncation radius (Martin et al. 2023). It strongly supports that there is likely a highly misaligned circumbinary planet which is located inside the disk around AC Her. A promising technique to detect misaligned CBPs is to measure binary eclipse timing variations (ETVs) (Sybilski et al. 2010). Applications of ETVs show that binary systems KIC 5095269, KIC 07177553 and KIC 7821010 hold inclined planetary mass objects around them (Borkovits et al. 2016; Getley et al. 2017). With the improvement of ETVs, it is believed that additional highly misaligned (even polar) CBPs around eccentric binaries or multiples with longer periods may be detected by taking advantage of such a technique based on future observations (Zhang & Fabrycky 2019).

In this work, we study dynamical structures of misaligned CBPs around eccentric binaries in a large parameter space (producing a global picture for the dynamics of CBPs) and then provide analytical understanding about those structures. The purpose of this work is to understand the dynamics of misaligned orbits under different circumbinary systems in order to make predictions about parameter space where the inner eccentric binary can host planets as long as possible. We approximate the dynamical model for describing CBPs as a hierarchical three-body problem, where the planet is treated as an outer test particle (Li et al. 2014; de Elia et al. 2019; Vinson & Chiang 2018; Naoz et al. 2017). The secular dynamics under hierarchical three-body configurations has been investigated extensively in the literature, where the eccentric von Zeipel-Lidov-Kozai (ZLK) mechanism is effective in understanding different astrophysical phenomena (Ford et al. 2000; Katz et al. 2011; Lithwick & Naoz 2011; Naoz et al. 2013; Li et al. 2014; Naoz 2016). Those short-range forces, such as general relativity effect, could significantly influence the eccentric ZLK effects (Naoz et al. 2013, 2017; Liu et al. 2015; Lepp et al. 2022). For the P-type configuration, it is known that the inverse ZLK resonance appears at the hexadecapolar-level Hamiltonian (de Elia et al. 2019; Vinson & Chiang 2018). Therefore, in the present work the secular approximation is formulated up to the hexadecapolar order in semimajor axis ratio in order to cover the effects caused by inverse ZLK resonance. Dynamical maps in the entire parameter space are produced by taking the second-derivative-based indicator $||\Delta D||$ as index and complex structures can be found in dynamical maps. Analytical study based on perturbative treatments is performed to understand numerical structures.

The remaining part of this work is organised as follows. In Sect. 2, the Hamiltonian model at the hexadecapolar-level approximation is formulated and validated. Varieties of stability conditions are briefly discussed in Sect. 3 and dynamical maps are produced in Sect. 4. In Sect. 5, dynamics under the quadrupole-order Hamiltonian is investigated

and applications of resonance curves to numerical structures are performed in Sect. 6. In Sect. 7, dynamics of secondary resonances is studied by means of perturbative treatments. Conclusions are summarised in Sect. 8.

2 HAMILTONIAN MODEL

In this work, we consider secular dynamics of CBPs. To this end, planets are approximated as exterior (massless) test particles in a hierarchical three-body configuration, where the inner binary is composed of a central object with mass m_0 and an inner perturber with mass m_1 . The gravitational influence upon the binary stars coming from the test particle is negligible (i.e., the so-called test-particle approximation), thus the inner binary moves around their barycentre on a fixed Keplerian orbit. Please refer to Fig. 1 for the schematic diagram of dynamical model. Similar configuration has been considered in previous works for studying secular dynamics of exterior test particles (de Elia et al. 2019; Naoz et al. 2017; Vinson & Chiang 2018).

As usual, we adopt the Jacobi coordinates to describe the motion of the perturber and test particles, i.e., the inner perturber m_1 moves around the central object m_0 and the test particle moves around the barycentre of the inner binary. To characterise their orbits, the following orbital elements are used: the semimajor axis $a_{1,2}$, eccentricity $e_{1,2}$, inclination $i_{1,2}$, longitude of ascending node $\Omega_{1,2}$, argument of pericentre $\omega_{1,2}$ and mean anomaly $M_{1,2}$. Unless otherwise stated, the subscript ‘1’ stands for the variables of the perturber and the subscript ‘2’ represents the variables of test particles.

Considering the fact that the perturber’s orbit corresponds to the invariant plane of system, we choose an inertial m_0 -centred coordinate reference frame with the invariant plane as the x - y plane and the angular momentum vector of system as the z -axis, leading to $i_1 = 0$. Without loss of generality, the x -axis is directed toward the perturber’s pericentre, which means $\varpi_1 (= \omega_1 + \Omega_1) = 0$. Please refer to Fig. 1 for the definition of coordinate system.

Under the test-particle assumption, the perturber’s orbit remains stationary. Thus, the orbital elements a_1 and e_1 are constant. Under hierarchical configurations, the semimajor axis ratio $\alpha = a_1/a_2$ is a small parameter, thus the disturbing function from the inner perturber can be expanded as a power series in α (i.e., Legendre expansion of disturbing function). As a result, the (unit mass) Hamiltonian, governing the evolution of test particles, can be written as (Harrington 1968, 1969)

$$\mathcal{H} = -\frac{\mathcal{G}(m_0 + m_1)}{2a_2} - \frac{\mathcal{G}m_0m_1}{a_2(m_0 + m_1)} \sum_{n=2}^N \left(\frac{a_1}{a_2}\right)^n \times \frac{m_0^{n-1} - (-m_1)^{n-1}}{(m_0 + m_1)^{n-1}} \left(\frac{r_1}{a_1}\right)^n \left(\frac{a_2}{r_2}\right)^{n+1} P_n(\cos\psi) \quad (1)$$

where \mathcal{G} is the Universal gravitational constant, r_1 is the distance between m_0 and m_1 , r_2 is the distance between the test particle and the barycentre of the inner binary and the angle ψ stands for the relative angle between the radius vectors of the test particle and the perturber (see Fig. 1 for details). $P_n(\cos\psi)$ is the Legendre polynomial of order n . In particular, the Hamiltonian represented by equation (1)

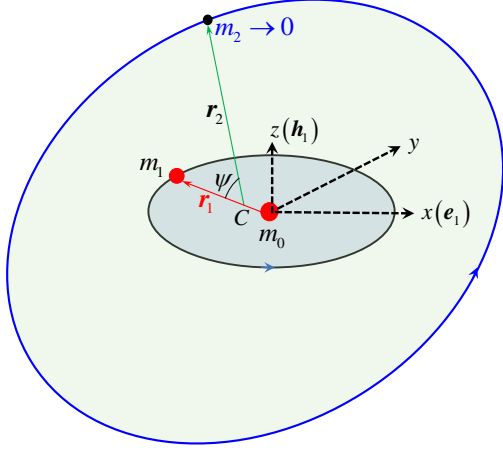


Figure 1. Schematic diagram for the geometric configuration of circumbinary planetary system and definitions of variables adopted in this work. The circumbinary planet is approximated as a test particle (i.e., $m_2 \rightarrow 0$), whose long-term dynamics is governed by the gravitational attraction from the inner binary with mass m_0 and m_1 . The barycentre of the inner binary is denoted by C. The invariant plane-based right-handed coordinate system O - xyz is defined with the origin at the location of m_0 , the x -axis aligned with the pericentre vector of m_1 and the z -axis along with its angular momentum vector. The position vector from m_0 towards m_1 is denoted by \mathbf{r}_1 , the position vector from C towards m_2 is denoted by \mathbf{r}_2 (Jacobi coordinates), and their relative angle is ψ .

is referred to as quadrupole-level approximation when the truncated order is taken as $N = 2$, as octupole-level approximation when $N = 3$, as hexadecapolar-level approximation when $N = 4$, and so on.

In long-term evolutions, the short-term influences associated with the mean motion of the test particle and the inner perturber can be filtered out by means of double-averaging technique (Naoz 2016). Such a similar phase-averaged or secular approximation can be found in Lei (2020) and Lei et al. (2022) for studying secular dynamics of navigation satellites. Performing double averages for the Hamiltonian and truncating it at the hexadecapolar order, we can get the resulting double-averaged Hamiltonian as

$$\mathcal{H} = -\mathcal{C}_0 (F_2 + \varepsilon_1 F_3 + \varepsilon_2 F_4), \quad (2)$$

where the constant terms have been removed. In the averaged Hamiltonian, the mean anomalies $M_{1,2}$ become cyclic variables and thus the semimajor axes $a_{1,2}$ are constants during the long-term evolution. In equation (2), the coefficient \mathcal{C}_0 is given by

$$\mathcal{C}_0 = \frac{\mathcal{G}m_0m_1}{16(m_0+m_1)} \frac{a_1^2}{a_2^3},$$

which remains unchanged during the long-term evolution, the quadrupole-order term is

$$F_2 = \frac{1}{(1-e_2^2)^{3/2}} [(2+3e_1^2)(3\theta^2-1) + 15e_1^2(1-\theta^2)\cos(2\Omega_2)]$$

the octupole-order term is

$$F_3 = -\frac{15}{32} \frac{e_1e_2}{(1-e_2^2)^{5/2}} \left\{ (4+3e_1^2) \times \right. \\ \left. [(-1+11\theta+5\theta^2-15\theta^3)\cos(\Omega_2-\omega_2) \right. \\ \left. + (-1-11\theta+5\theta^2+15\theta^3)\cos(\Omega_2+\omega_2)] \right. \\ \left. + 35e_1^2 [(1-\theta-\theta^2+\theta^3)\cos(3\Omega_2-\omega_2) \right. \\ \left. + (1+\theta-\theta^2-\theta^3)\cos(3\Omega_2+\omega_2)] \right\}$$

and the hexadecapolar-order term is

$$F_4 = \frac{15}{64} \frac{2+3e_2^2}{(1-e_2^2)^{7/2}} \left\{ d_1 - 11 - 18\theta^2 + 21\theta^4 \right. \\ \left. - 4d_2(1-8\theta^2+7\theta^4)\cos(2\Omega_2) \right. \\ \left. + 7d_3(1-2\theta^2+\theta^4)\cos(4\Omega_2) \right\} \\ + \frac{15}{64} \frac{e_2^2}{(1-e_2^2)^{7/2}} \left\{ -6(1-8\theta^2+7\theta^4)\cos(2\omega_2) \right. \\ \left. + 4d_2(1+5\theta-6\theta^2-7\theta^3+7\theta^4)\cos(2\Omega_2-2\omega_2) \right. \\ \left. + 4d_2(1-5\theta-6\theta^2+7\theta^3+7\theta^4)\cos(2\Omega_2+2\omega_2) \right. \\ \left. + 7d_3(1-2\theta+2\theta^3-\theta^4)\cos(4\Omega_2-2\omega_2) \right. \\ \left. + 7d_3(1+2\theta-2\theta^3-\theta^4)\cos(4\Omega_2+2\omega_2) \right\}$$

where $\theta = \cos i_2$ and the constant coefficients $d_{1,2,3}$ in the expression of F_4 are given by

$$d_1 = \frac{64}{5} + 24e_1^2 + 9e_1^4,$$

$$d_2 = \frac{21}{8} (2e_1^2 + e_1^4),$$

$$d_3 = \frac{63}{8} e_1^4.$$

The factors ε_1 and ε_2 stand for the significance of the octupole-order and hexadecapolar-order contributions compared to the quadrupole-order term, given by

$$\varepsilon_1 = \frac{m_0 - m_1}{m_0 + m_1} \frac{a_1}{a_2}, \quad \varepsilon_2 = \frac{m_0^3 + m_1^3}{(m_0 + m_1)^3} \frac{a_1^2}{a_2^2}$$

It is observed that ε_1 is proportional to the semimajor axis ratio $\alpha = a_1/a_2$ and ε_2 is proportional to α^2 . In particular, when the inner binary is of equal mass (i.e., $m_0 = m_1$), the octupole-order term disappears because of $\varepsilon_1 = 0$, and the hexadecapolar-order term takes its minimum.

One remark is made here. The Hamiltonian at the hexadecapolar-level approximation given here is confirmed to be in agreement with the ones presented in Vinson & Chiang (2018) and de Elia et al. (2019) and the octupole-order version is in agreement with the one given in Naoz et al. (2017), but with different expressions.

As the coefficient \mathcal{C}_0 is a constant during the long-term evolution, it is convenient to normalise the Hamiltonian by \mathcal{C}_0 as follows¹:

$$\mathcal{H} = -F_2 - \varepsilon_1 F_3 - \varepsilon_2 F_4 \\ = \mathcal{H}_0(e_2, i_2, \Omega_2) + \varepsilon \mathcal{H}_1(e_2, i_2, \Omega_2, \omega_2) \quad (3)$$

where $\mathcal{H}_0 = -F_2$ and $\varepsilon \mathcal{H}_1 = -\varepsilon_1 F_3 - \varepsilon_2 F_4$. From the viewpoint of perturbation theory, the Hamiltonian \mathcal{H}_0

¹ Normalisation of Hamiltonian is equivalent to re-scaling the unit of time.

(quadrupole-level approximation) describes the unperturbed dynamics and the Hamiltonian \mathcal{H}_1 plays a role of perturbation which is dependent on ε_1 and ε_2 .

To study the long-term evolution from the viewpoint of Hamiltonian, we introduce the normalised Delaunay variables:

$$g_2 = \omega_2, \quad G_2 = \sqrt{1 - e_2^2}, \\ h_2 = \Omega_2, \quad H_2 = G_2 \cos i_2.$$

In terms of Delaunay variables, the normalised Hamiltonian is expressed as

$$\mathcal{H} = \mathcal{H}_0(G_2, H_2, h_2) + \varepsilon \mathcal{H}_1(G_2, g_2, H_2, h_2). \quad (4)$$

The Hamiltonian canonical relation leads to the equations of motion (Morbidelli 2002)

$$\frac{dg_2}{d\tau} = \frac{\partial \mathcal{H}}{\partial G_2}, \quad \frac{dh_2}{d\tau} = \frac{\partial \mathcal{H}}{\partial H_2}, \\ \frac{dG_2}{d\tau} = -\frac{\partial \mathcal{H}}{\partial g_2}, \quad \frac{dH_2}{d\tau} = -\frac{\partial \mathcal{H}}{\partial h_2}, \quad (5)$$

and the associated Lagrange planetary equations in terms of orbit elements can be written as (Murray & Dermott 1999)

$$\frac{de_2}{d\tau} = \frac{\eta}{e_2} \frac{\partial \mathcal{H}}{\partial \omega_2}, \\ \frac{di_2}{d\tau} = \frac{\csc i_2}{\eta} \left(\frac{\partial \mathcal{H}}{\partial \Omega_2} - \cos i_2 \frac{\partial \mathcal{H}}{\partial \omega_2} \right), \\ \frac{d\Omega_2}{d\tau} = -\frac{\csc i_2}{\eta} \frac{\partial \mathcal{H}}{\partial i_2}, \\ \frac{d\omega_2}{d\tau} = \frac{\cot i_2}{\eta} \frac{\partial \mathcal{H}}{\partial i_2} - \frac{\eta}{e_2} \frac{\partial \mathcal{H}}{\partial e_2} \quad (6)$$

where $\eta = \sqrt{1 - e_2^2}$. The relationship between the time τ under the normalised Hamiltonian and the time t under the non-normalised Hamiltonian is given by

$$\tau = \frac{C_0}{\sqrt{\mathcal{G}}(m_0 + m_1) a_2} t \\ = \frac{\mathcal{G} m_0 m_1}{16(m_0 + m_1)} \frac{a_1^2}{a_2^3} \frac{1}{\sqrt{\mathcal{G}}(m_0 + m_1) a_2} t.$$

In Fig. 2, time histories of eccentricity and inclination are compared for the trajectories numerically propagated under the non-averaged dynamical model (direct N-body integration) and under the double-averaged model up to the hexadecapolar order (secular approximation). Please refer to the caption for detailed setting of system parameters as well as initial condition. It is observed that (a) the evolution under the non-averaged model exhibits short-term oscillations, while the short-term oscillations are filtered out under the double-averaged Hamiltonian model, (b) variation of inclination presents good periodicity as the evolution of inclination is dominated by the integrable quadrupole-order Hamiltonian, and (c) there are good agreements between the N-body integration results and secular approximations for the long-term evolution. As a result, secular approximation up to hexadecapolar order is effective to predict long-term evolution for CBPs.

Without otherwise stated, it is assumed that the central object holds the mass of $m_0 = 1.0 m_\odot$ and the semimajor axes of the inner and outer orbits are taken as $a_1 = 3$ au and $a_2 = 40$ au in the entire work. It means that the semimajor axis ratio is fixed at $\alpha = 3/40$.

3 STABILITY CONDITION

It is of significance to perform stability analysis of multi-body systems in order to answer the question: in what regions of parameter space can CBPs persist for a long enough time? About this topic, Dvorak et al. (1989) numerically derived stability limits of outer planetary orbits (P-types) in binary systems, then Holman & Wiegert (1999) provided an empirical expression for the critical semimajor axis $a_{2,c}$ as a function of binary mass fraction μ_b and eccentricity e_1 . Extending to 3D space, Doolin & Blundell (2011) performed a numerical investigation about the stability of test-particle CBPs in circumbinary phase space as a function of binary eccentricity e_1 and mass fraction μ_b and discovered that circumbinary orbits are surprisingly stable throughout the parameter space (e_1, μ_b) . With a given pair of (e_1, μ_b) , complex structures can be further observed in the (a_2, i_2) space. Chen et al. (2019) and Chen et al. (2020) extended the study of Doolin & Blundell (2011) to the non-zero mass case and they systematically explored the dependence of stability of nearly circular bots upon binary eccentricity e_1 , binary mass fraction μ_b , planet mass m_2 , planet semimajor axis a_2 , and planet inclination i_2 based on a large number of numerical simulations. Similarly, complex structures are observed in the (a_2, i_2) space. Based on ~ 150 million full N-body simulations, Quarles et al. (2018) developed numerical tools for quick, easy, and accurate determination of stability limit in the (e_1, μ_b) space and, in particular, they provided open-source python software to make use of their simulations. Recently, Georgakarakos et al. (2024) revisited the problem of dynamical stability of 3D and eccentric circumbinary planetary orbits by performing more than 3×10^8 numerical simulations and they provided empirical expressions in the form of multidimensional and parameterised fits for stability limits.

There are many works in studying long-term stability of planets moving in binary systems, and varieties of stability conditions can be found in previous literature under different assumptions. In this section, we briefly review them under the unified notation system adopted in this work (see Fig. 1 for the configuration) and then make a direct comparison with applications to CBPs.

For co-planar and nearly circular planetary orbits, Dvorak et al. (1989) provided a stability criterion where the semimajor axis of the lower critical orbit is a function of a_1 and e_1 in the following form:

$$a_{2,c} = a_1 (2.37 + 2.76e_1 - 1.04e_1^2) \quad (7)$$

which is independent on the mass parameter of the inner binary $\mu_b = m_1/(m_0 + m_1)$, planetary eccentricity and inclination (e_2 and i_2). If a_2 is greater than the critical value $a_{2,c}$, the associated system is unstable.

The influence of the mass parameter of binary (μ_b) is considered in Holman & Wiegert (1999), who presented a widely used stability condition for P-type configurations as follows:

$$a_{2,c} = a_1 (1.6 + 5.1e_1 - 2.22e_1^2 + 4.12\mu_b - 4.27e_1\mu_b \\ - 5.09\mu_b^2 + 4.61e_1^2\mu_b^2) \quad (8)$$

which is updated by Quarles et al. (2018) in the following

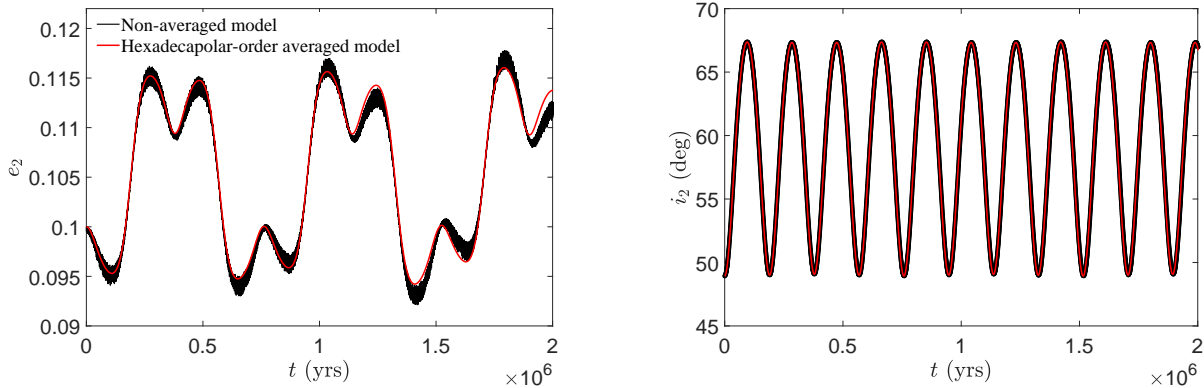


Figure 2. Comparison between the N-body integration results (black lines) and the secular approximation at the hexadecapolar order (red lines) over 2×10^6 yrs. The left panel is for the evolution of eccentricity e_2 and the right panel is for the evolution of inclination i_2 . In practical simulations, the system parameters are taken as $m_0 = 1.0m_\odot$, $m_1 = 0.5m_\odot$, $a_1 = 3\text{au}$ and $a_2 = 40\text{au}$; in this case it holds $C_0 = 2.9296875 \times 10^{-6}$, $\varepsilon_1 = 2.5 \times 10^{-2}$ and $\varepsilon_2 = 1.875 \times 10^{-3}$. Under the test-particle approximation, the eccentricity of the inner body remains constant and it is taken as $e_1 = 0.3$ in practice. The initial conditions of both trajectories are set as $e_{2,0} = 0.1$, $i_{2,0} = 48.925^\circ$ and $\Omega_{2,0} = \omega_{2,0} = \pi/2$ (the slight difference between the ‘mean’ and ‘osculating’ elements at the initial instant is ignored). Good agreement can be observed between the trajectories propagated under the non-averaged model and the averaged model truncated at the hexadecapolar order.

form (see their Fit 1):

$$a_{2,c} = a_1 (1.48 + 3.92e_1 - 1.41e_1^2 + 5.14\mu_b + 0.33e_1\mu_b - 7.95\mu_b^2 - 4.89e_1^2\mu_b^2). \quad (9)$$

Both expressions in [Holman & Wiegert \(1999\)](#) and [Quarles et al. \(2018\)](#) are independent on planetary eccentricity and inclination (e_2 and i_2), thus they are suitable for low-inclination and low-eccentricity planetary orbits under P-type configurations.

Considering the influence of planetary eccentricity e_2 upon stability condition, [Adelbert et al. \(2023\)](#) provided a stability criterion as follows:

$$a_{2,c} = \frac{a_1}{1 - e_2} [1.36 + 5.79e_1 - 5.87e_1^2 + 1.99\mu_b - 3.14\mu_b^2 + (1.85 - 2.1e_1^2 + 3e_1\mu_b) e_2] \quad (10)$$

where the influence of planetary inclination i_2 is not considered. Thus, the stability condition given by equation (10) is suitable for low-inclination planetary orbits.

Furthermore, considering the influence of planetary eccentricity e_2 and inclination i_2 , [Mardling & Aarseth \(2001\)](#) presented a simple stability criterion (in the test-particle approximation with $m_2 \rightarrow 0$),

$$a_{2,c} = 2.8a_1 \frac{(1 + e_2)^{2/5}}{(1 - e_2)^{6/5}} \left(1 - 0.3 \frac{i_2}{\pi}\right) \quad (11)$$

and recently [Georgakarakos et al. \(2024\)](#) provided a generalised stability criterion which is suitable for a large-range parameter space ($e_2 < 0.8$) as follows:

$$\begin{aligned} \log_{10} a_{2,c} = & \log_{10} a_1 + 0.23612 - 0.29377 (\log_{10} \mu_b) + 0.2271 i_2 \\ & + 1.06753 e_1 + 0.62109 e_2 - 0.21512 (\log_{10} \mu_b)^2 \\ & - 0.06648 i_2^2 - 1.52936 e_1^2 - 0.4748 e_2^2 - 0.31329 e_1 i_2 \\ & - 0.00869 e_2 i_2 + 0.11846 e_1 i_2^2 - 0.03932 (\log_{10} \mu_b)^3 \\ & - 0.00933 i_2^3 + 0.87506 e_1^3 + 1.25895 e_2^3. \end{aligned}$$

It is noted that planetary inclination i_2 in both Eqs. (11) and (12) is given in unit of radian. The stability condition of [Mardling & Aarseth \(2001\)](#) does not consider the influence of mass parameter μ_b and binary’s eccentricity e_1 . From the stability condition given by [Georgakarakos et al. \(2024\)](#), it is observed that the critical semimajor axis $a_{2,c}$ is a function of a_1 , μ_b , e_1 , e_2 and i_2 , which is available for varieties of configurations. Please refer to [Georgakarakos et al. \(2024\)](#) for the stability criterion about arbitrary planetary eccentricities and its applications to those CBPs observed so far.

To make a direct comparison among different versions of stability condition, we take a representative circumbinary planetary system with $m_0 = 1.0m_\odot$ and $m_1 = 0.5m_\odot$ as an example. The results are shown in Fig. 3. The detailed setting of other parameters are provided on the top of each figure. In the (e_1, a_2) space, $a_{2,c}$ is an increasing function of e_1 except for the curve given by [Adelbert et al. \(2023\)](#). In the (e_2, a_2) space, the curve of [Mardling & Aarseth \(2001\)](#) agrees well with that of [Adelbert et al. \(2023\)](#) in the low-eccentricity space and agrees with that of [Georgakarakos et al. \(2024\)](#) in the high-eccentricity space. Only [Mardling & Aarseth \(2001\)](#) and [Georgakarakos et al. \(2024\)](#) can provide the stability dependence on planetary inclination i_2 , and the last two panels of Fig. 3 provide their stability curves in the (i_2, a_2) and (i_2, e_2) space. It is observed that the critical curves of [Mardling & Aarseth \(2001\)](#) are linear functions of inclination i_2 , while the curves of [Georgakarakos et al. \(2024\)](#) present nonlinear behaviours: (a) $a_{2,c}$ increases first and then decreases with i_2 and (b) $e_{2,c}$ decreases first and then increases with i_2 .

In the following simulations, we need to ensure that the system parameters satisfy the stability condition. In practice, we adopt the stability limit given by [Mardling & Aarseth \(2001\)](#). Numerical simulations are stopped when

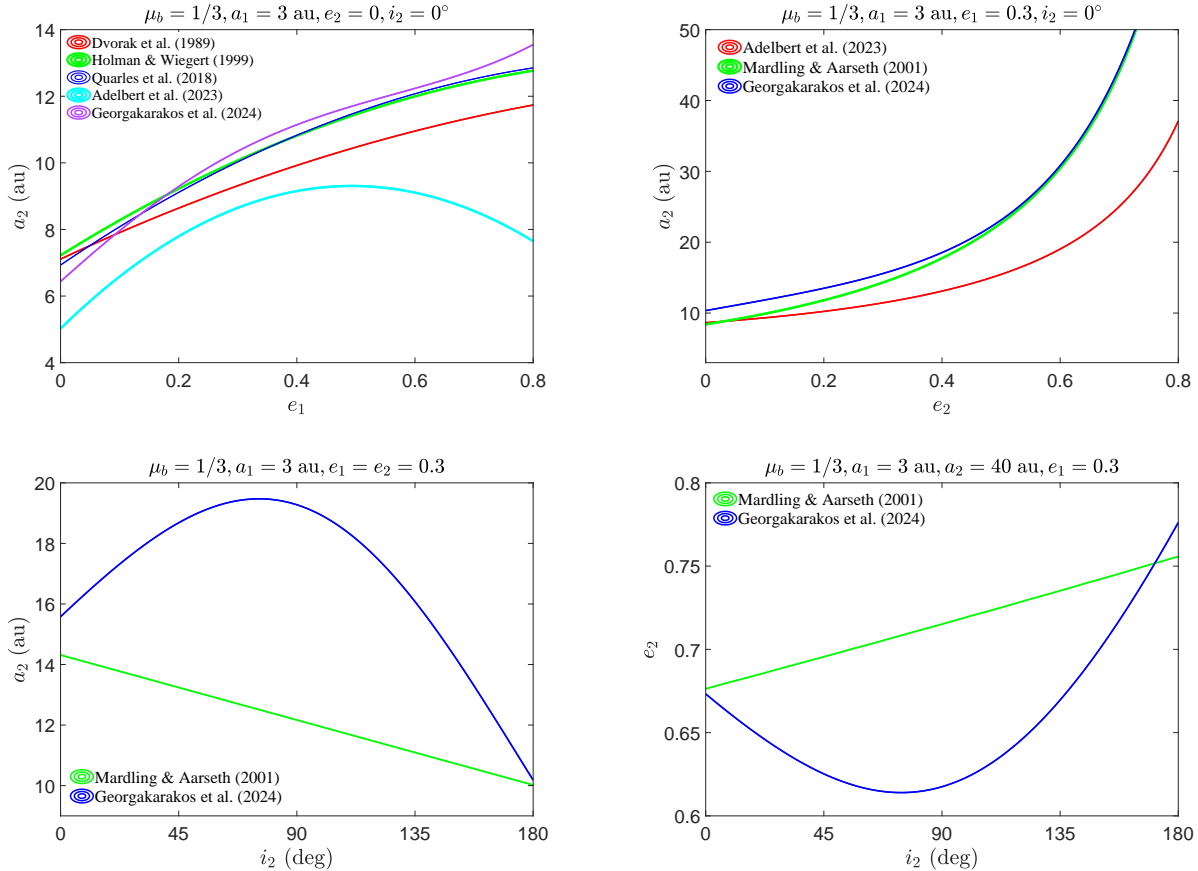


Figure 3. Comparisons among critical curves of stability. The points located below the critical curves are stable. The stability criteria shown here come from [Dvorak et al. \(1989\)](#), [Holman & Wiegert \(1999\)](#), [Mardling & Aarseth \(2001\)](#), [Quarles et al. \(2018\)](#), [Adelbert et al. \(2023\)](#) and [Georgakarakos et al. \(2024\)](#).

stability condition is violated. Results remain qualitatively unchanged if a different stability condition is taken.

4 DYNAMICAL STRUCTURES

In this section, phase-space structures of CBPs under hierarchical three-body configurations are numerically explored by taking advantage of dynamical maps, which provide a global view about the dynamics. The indicator we adopt for producing dynamical maps is the second-derivative-based index $\|\Delta D\|$ where D is the action diameter of an orbit. This indicator was recently developed by [Daquin & Charalambous \(2023\)](#) and it is a sensitive and robust index for detecting separatrices, resonant centre and chaotic motion in the phase space. Especially, this indicator has a strong ability for distinguishing minute structures caused by high-order or secondary resonances ([Lei 2024](#); [Huang & Lei 2024](#)). The introduction of $\|\Delta D\|$ follows from the same authors' recent developments on Lagrangian descriptors and arc-length of orbits ([Daquin et al. 2022](#)). Compared to other Chaotic index (e.g., fast Lyapunov indicator), the computation of $\|\Delta D\|$ is free of tangent dynamics ([Guzzo et al. 2002](#); [Daquin & Charalambous 2023](#)).

As for the current problem, the diameter metric of an

orbit is defined by

$$D(e_{2,0}, i_{2,0}, \Omega_{2,0}, \omega_{2,0}) = \|(\delta e_2, \delta i_2)\|_\infty \quad (13)$$

where $(e_{2,0}, i_{2,0}, \Omega_{2,0}, \omega_{2,0})$ is the initial state, δe_2 and δi_2 represent the amplitude of the eccentricity and inclination over a given period of time t_{\max} , determined by

$$\begin{aligned} \delta e_2(e_{2,0}, i_{2,0}, \Omega_{2,0}, \omega_{2,0}) &= \max_{0 \leq t \leq t_{\max}} e_2(e_{2,0}, i_{2,0}, \Omega_{2,0}, \omega_{2,0}, t) \\ &\quad - \min_{0 \leq t \leq t_{\max}} e_2(e_{2,0}, i_{2,0}, \Omega_{2,0}, \omega_{2,0}, t) \end{aligned}$$

and

$$\begin{aligned} \delta i_2(e_{2,0}, i_{2,0}, \Omega_{2,0}, \omega_{2,0}) &= \max_{0 \leq t \leq t_{\max}} i_2(e_{2,0}, i_{2,0}, \Omega_{2,0}, \omega_{2,0}, t) \\ &\quad - \min_{0 \leq t \leq t_{\max}} i_2(e_{2,0}, i_{2,0}, \Omega_{2,0}, \omega_{2,0}, t) \end{aligned}$$

Based on the diameter D , [Daquin & Charalambous \(2023\)](#) defined a second-derivative-based index $\|\Delta D\|$ as follows:

$$\|\Delta D\| = \left| \frac{\partial^2 D}{\partial e_{2,0}^2} \right| + \left| \frac{\partial^2 D}{\partial i_{2,0}^2} \right| + \left| \frac{\partial^2 D}{\partial \Omega_{2,0}^2} \right| + \left| \frac{\partial^2 D}{\partial \omega_{2,0}^2} \right|. \quad (14)$$

For the current problem, it is found that the last two terms have small contribution to $\|\Delta D\|$. To save computational cost, $\|\Delta D\|$ is simplified to be

$$\|\Delta D\| = \left| \frac{\partial^2 D}{\partial e_{2,0}^2} \right| + \left| \frac{\partial^2 D}{\partial i_{2,0}^2} \right|, \quad (15)$$

where the second-order derivative $\frac{\partial^2 D}{\partial x^2}$ can be numerically calculated by means of central difference

$$\frac{\partial^2 D}{\partial x^2} = \frac{D(x+h) + D(x-h) - 2D(x)}{h^2}$$

where x stands for $e_{2,0}$ or $i_{2,0}$, and h is the associated step. Please refer to [Daquin & Charalambous \(2023\)](#) for more details about the definition, determination and applications of the indicator $\|\Delta D\|$.

Our recent works show that a normalised second-derivative-based index has a stronger ability to detect those structures with small strength ([Lei 2024; Huang & Lei 2024](#)). Following the same consideration, we introduce the normalised indicator $\|\Delta D\|$ as follows:

$$\|\Delta D\| = \frac{1}{D} \left(\left| \frac{\partial^2 D}{\partial e_{2,0}^2} \right| + \left| \frac{\partial^2 D}{\partial i_{2,0}^2} \right| \right) \quad (16)$$

According to the definition of $\|\Delta D\|$, it measures the relative continuity of the distance metric D in the considered phase space. Thus, it becomes possible to take $\|\Delta D\|$ to detect the separatrix crossing, meaning that the dynamical structures with $\|\Delta D\|$ as indicator could provide minute structures in the phase space.

To produce dynamical maps with $\|\Delta D\|$ as chaotic index, the initial longitude of ascending node and argument of pericentre are assumed as $\Omega_{2,0} = \omega_{2,0} = \pi/2$. Such a choice of initial angles is based on the following considerations: (a) $\Omega_2 = \pi/2$ is the centre of nodal librating trajectory (see Sect. 5), (b) $\omega_2 = \pi/2$ is the centre of inverse ZLK librating trajectory, and (c) it leads to $\varpi = \pi$ or $\varpi = 0$, which corresponds to an initial aligned or anti-aligned configuration. Thus, this choice can represent almost all types of trajectories in the considered phase space. By fixing the initial angles (this is similar to taking a snapshot for a beam of Hamiltonian flow), it becomes possible for us to explore dynamical structures in the action space. Our practical experiments indicate that dynamical structures are weakly related to planetary eccentricity e_2 , thus without loss of generality we take $e_{2,0} = 0.1$ in simulations. The planetary inclination i_2 and binary's eccentricity e_1 are distributed in the domain $[0^\circ, 180^\circ] \times [0, 0.9]$ with steps of $\delta i_2 = 0.2^\circ$ and $\delta e_1 = 0.01$. Numerical simulations are stopped if any one of the following conditions is satisfied: (a) the integration time is over 200π normalised units of time ($t_{\max} \sim 100$ period of Ω_2); (b) the stability condition given by [Mardling & Aarseth \(2001\)](#) is violated; (c) the time step of numerical integration is smaller than 1.0×10^{-8} . Almost all simulations are stopped due to condition (a).

Dynamical maps in the (i_2, e_1) space are shown in Fig. 4 for different mass parameters $\mu_b = m_1/(m_0 + m_1)$. In particular, the cases of $m_1 = 0.1m_\odot, 0.5m_\odot, 1.0m_\odot, 2.0m_\odot, 5.0m_\odot, 10.0m_\odot$ are considered with the mass of the central object at $m_0 = 1.0m_\odot$. For convenience of display, the magnitude of $\|\Delta D\|$ is limited to the range of $[10^1, 10^5]$ and the index shown in the colour bar corresponds to the base 10 logarithm of $\|\Delta D\|$. The regions with higher $\|\Delta D\|$ are more chaotic.

From Fig. 4, it is observed that (a) there are complex structures arising in the dynamical maps, (b) dynamical maps with different mass parameters hold slightly different structures, showing that dynamical structures are weakly dependent on the mass parameter, (c) in each panel there is

a main V-shape structure which is symmetric with respect to the polar orbit, and (d) minute structures can be observed inside and outside the V-shape region, and they are no longer symmetric with respect to $i_2 = 90^\circ$ (i.e., symmetry breaking of minute structures). However, it is different for the case of $m_1 = 1.0m_\odot$ (equal-mass binary), where the minute structures inside and/or outside the V-shape region are nearly symmetric with respect to $i_2 = 90^\circ$ and they hold almost the same strength. This is because, in the equal-mass case, the octupole-order contribution disappears (see the Hamiltonian developed in Sect. 2), and all the substructures arising in the dynamical maps are attributed to the hexadecapolar-order terms, which are almost equal-strength.

Regarding dynamical maps, [Cuello & Giuppone \(2019\)](#) adopted the eccentricity variation Δe_2 of orbits as index (see their Fig. 6). In their dynamical maps, only the structures caused by 1:1 resonance can be observed but those minute structures caused by high-order and secondary resonances are not visible.

To understand the complex dynamical structures arising in Fig. 4, we take the configurations with $e_1 = 0.1$ and $e_1 = 0.3$ as examples to produce Poincaré sections, defined by

$$\omega_2 = \pi/2, \quad \dot{\omega}_2 > 0. \quad (17)$$

Under a given Hamiltonian, the points are recorded every time when CBPs pass through the section of $\omega_2 = \pi/2$ with positive angular velocity. For convenience, the Hamiltonian is characterised by the critical inclination $i_{2,c}$ in the form of $\mathcal{H}(\Omega_2 = \omega_2 = \pi/2, e_2 = 0.6, i_2 = i_{2,c})$. See Fig. 5 for Poincaré sections shown in the (Ω_2, i_2) space for the cases of $m_1 = 0.1m_\odot$ and $m_1 = 0.5m_\odot$. The initial angles of CBPs are assumed at $\Omega_{2,0} = \omega_{2,0} = \pi/2$. The index shown in the colour bar stands for the magnitude of planetary eccentricity e_2 , which is cut off to ensure the stability condition ([Mardling & Aarseth 2001](#)). It should be mentioned that the physically allowed region in the (Ω_2, i_2) space is determined by the given Hamiltonian \mathcal{H} , mass parameter μ_b , binary eccentricity e_1 , semimajor axis ratio $\alpha = a_1/a_2$ and stability limit. Please refer to the caption of Fig. 5 for the detailed setting of e_1 and $i_{2,c}$. To distinguish the regions of nodal libration and nodal circulation, dynamical separatrices under the quadrupole-order dynamical model are also shown in the Poincaré sections and they will be discussed in the next section.

When the eccentricity of the inner binary (e_1) is given, it is observed that Poincaré sections for the cases of $m_1 = 0.1m_\odot$ and $m_1 = 0.5m_\odot$ hold similar dynamical structures. However, when the mass parameter m_1 is given, dynamical structures arising in Poincaré sections are totally different for the cases of $e_1 = 0.1$ and $e_1 = 0.3$. It means that phase-space structures of CBPs are dominated by binary's eccentricity e_1 .

For the case of $e_1 = 0.1$, chaotic layers can be observed around the dynamical separatrix of nodal resonance. Outside the nodal libration zone, islands associated with high-order resonances can be found and, inside the nodal libration zone, islands associated with secondary resonances can be observed. The primary nodal resonance (quadrupole-order resonance), high-order and secondary resonances (octupole- and hexadecapolar-order resonances) are together responsi-

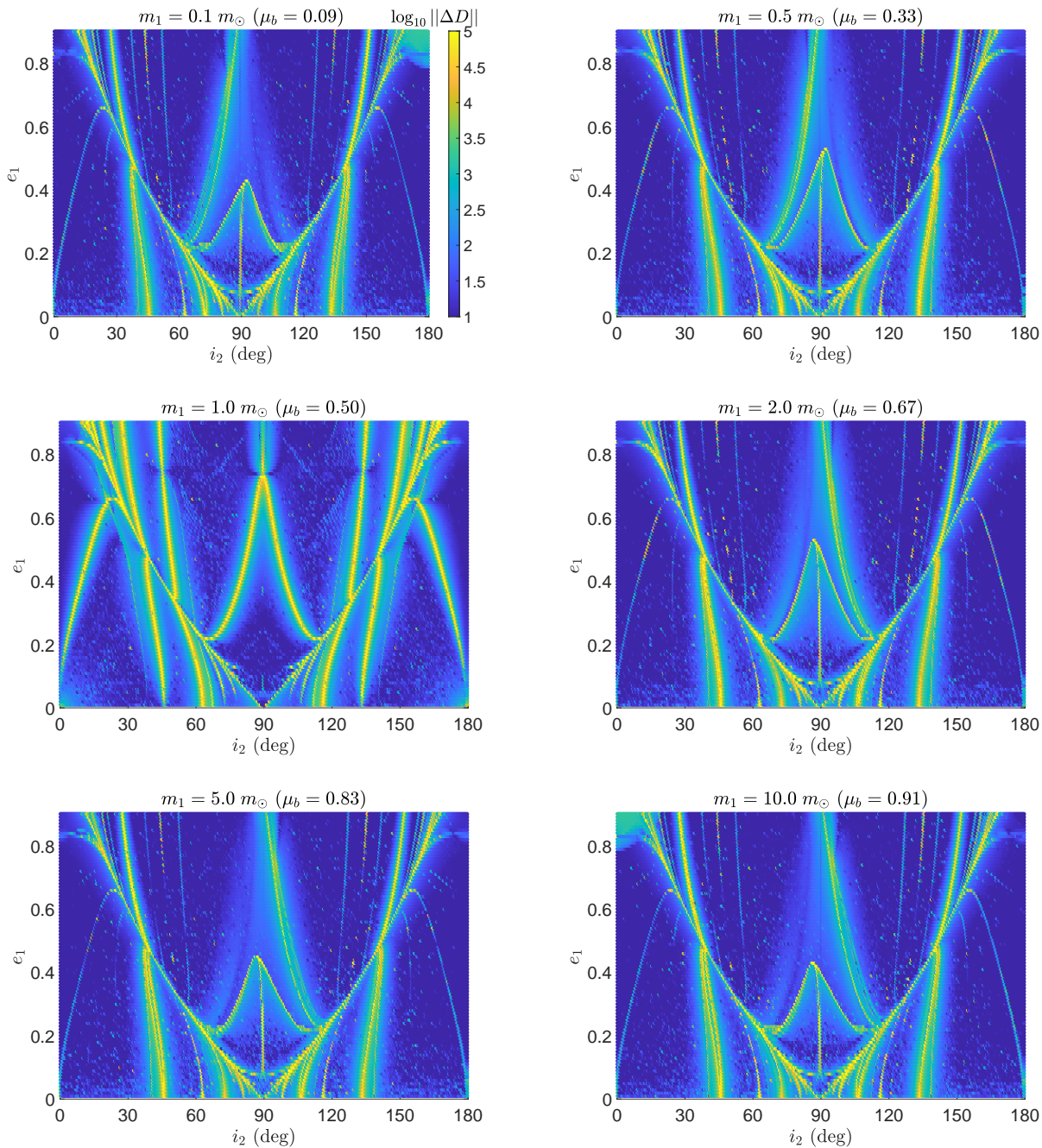


Figure 4. Dynamical maps with the normalised second-derivative-based index $\|\Delta D\|$ shown in the (i_2, e_1) parameter space for different mass parameters $\mu_b = m_1/(m_0+m_1)$ where m_0 is fixed as $m_0 = 1.0m_\odot$ and m_1 is given on the top of each panel. To produce the dynamical maps, the initial eccentricity of test particle is assumed at $e_{2,0} = 0.1$ (additional experiments show that different initial eccentricities $e_{2,0}$ lead to similar maps), and the initial argument of pericentre and longitude of ascending node are taken as $\Omega_{2,0} = \omega_{2,0} = \pi/2$ (please see the text for explanation why we choose such a pair of initial angles). For convenience of display, the magnitude of $\|\Delta D\|$ is limited to the range of $[10^1, 10^5]$ and the index shown in the colour bar corresponds to the base 10 logarithm of $\|\Delta D\|$. Higher magnitude of $\|\Delta D\|$ indicates that the associated orbit is more chaotic.

ble for the entire phase-space structures arising in Poincaré sections.

For the configuration of $e_1 = 0.3$, all the possible motion under the given Hamiltonian takes place inside the region bounded by the dynamical separatrix. In this case, islands associated with secondary 1:1 resonance can be observed

in the section. The nodal resonance in combination with secondary 1:1 resonance dominates the dynamical structures arising in the section.

A question arises: how do the nodal, high-order and secondary resonances sculpt the dynamical structures arising in dynamical maps? To answer this question, we will analyti-

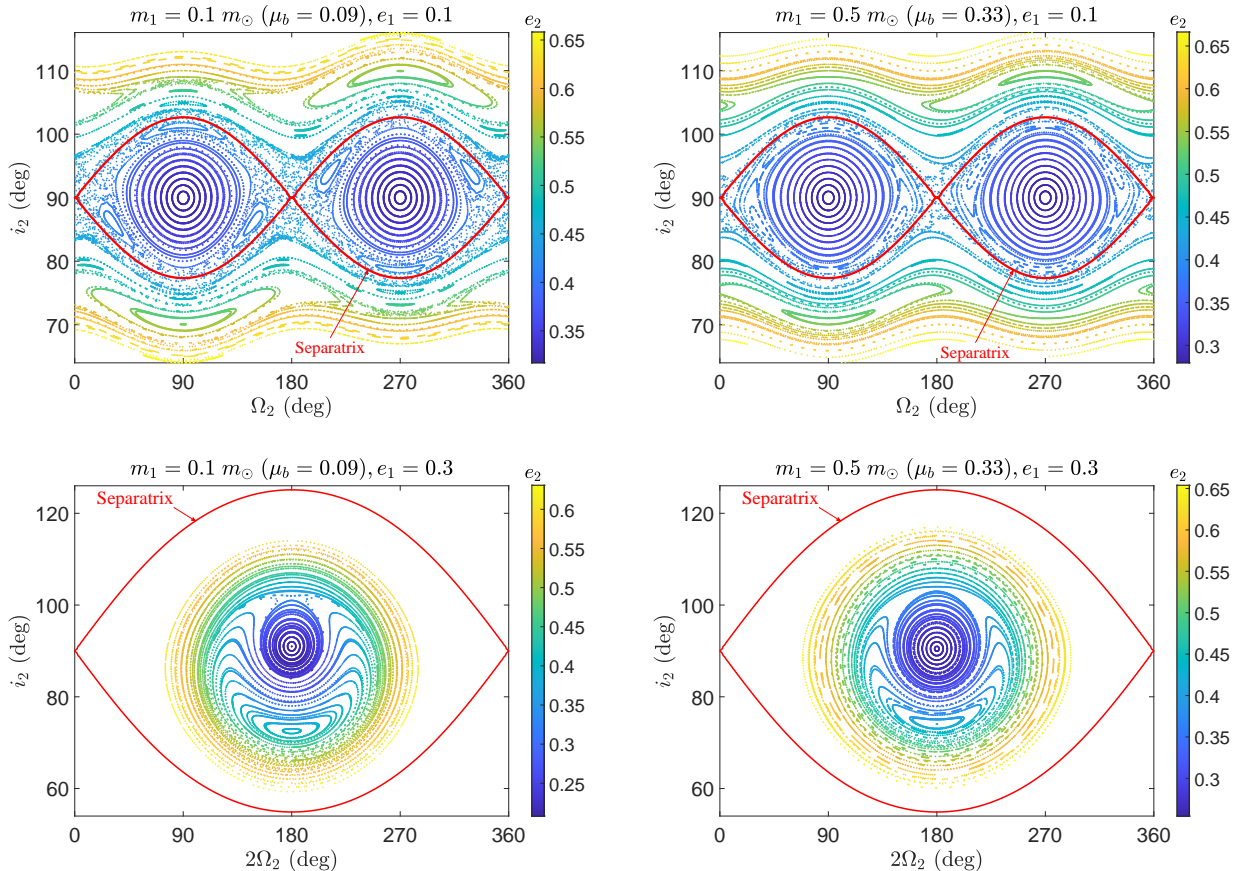


Figure 5. Poincaré surfaces of section, defined by $g_2 = \pi/2$ and $\dot{g}_2 > 0$. The index shown in the colour bar stands for the magnitude of e_2 . For producing Poincaré sections, the stability condition given by [Mardling & Aarseth \(2001\)](#) is satisfied. Hamiltonian is characterised by the critical inclination at $i_{2,c} = 67^\circ$ (top-two panels), at $i_{2,c} = 61^\circ$ (bottom-left panel) and at $i_{2,c} = 63^\circ$ (bottom-right panel). In the case of $e_1 = 0.1$ (see the top-row panels), islands associated with high-order and secondary resonances can be observed. In the case of $e_1 = 0.3$ (see the bottom-row panels), there are two libration islands inside the nodal libration region. The dynamical separatrix marked by red lines are determined by the quadrupole-level Hamiltonian, which is to be discussed in Sect. 5. The region bounded by dynamical separatrix is of nodal libration.

cally study the dynamics under the quadrupole-order model in Sect. 5, applications to numerical structures in Sect. 6 and then discuss secondary resonances under the hexadecapolar-order Hamiltonian model in Sect. 7 by taking advantage of perturbative treatments.

5 DYNAMICS OF THE QUADRUPOLE-ORDER MODEL

In this section, we concentrate on the dynamics under the quadrupole-order Hamiltonian model.

5.1 Phase portraits

At the quadrupole-level approximation, the Hamiltonian can be written as

$$\mathcal{H} = -\frac{1}{G_2^2} [(2 + 3e_1^2) (3H_2^2 - G_2^2) + 15e_1^2 (G_2^2 - H_2^2) \cos 2h_2]. \quad (18)$$

The angle g_2 is a cyclic variable, thus its conjugate momentum G_2 is a motion integral, showing that the planetary eccentricity e_2 remains constant under the quadrupole-order model. Considering the fact that the coefficient $\frac{1}{G_2^2}$ is constant, we can normalise the quadrupole-level Hamiltonian represented by equation (18) as

$$\mathcal{H} = -[(2 + 3e_1^2) (3H_2^2 - G_2^2) + 15e_1^2 (G_2^2 - H_2^2) \cos 2h_2]. \quad (19)$$

The resulting dynamical model is of one degree of freedom and thus it is integrable. In addition, the quadrupole-order Hamiltonian is independent on the mass parameter μ_b , thus we could conclude that μ_b has no influence on the dynamics of the quadrupole-order model. This is the reason that dynamical maps with different μ_b shown in Fig. 4 hold similar main structures. Analytical expressions of the nodal librating and circulating cycles under the quadrupole-level Hamiltonian are discussed in [Li et al. \(2014\)](#).

Phase-space structures can be explored by plotting level curves of Hamiltonian (i.e., phase portraits). Please see Fig. 6 for phase portraits under the quadrupole-order Hamilto-

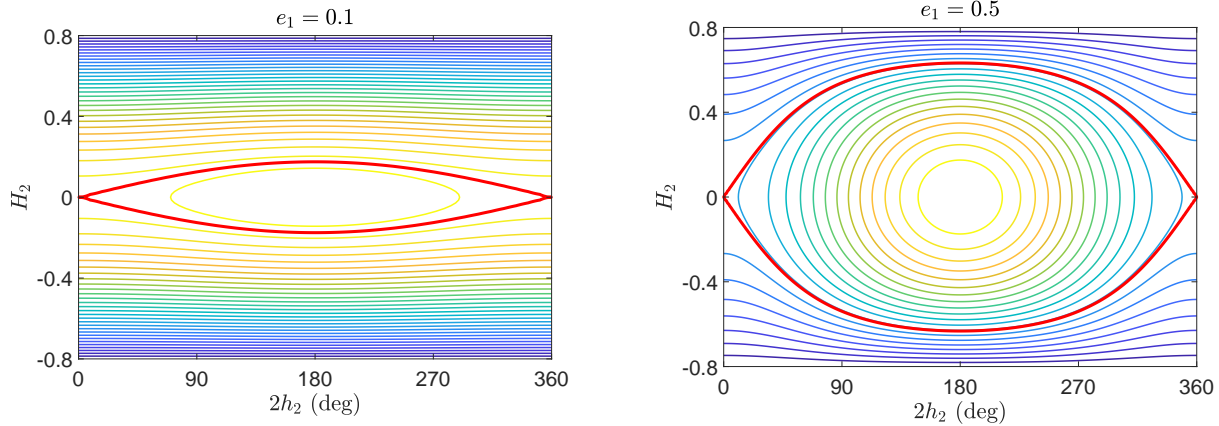


Figure 6. Phase diagrams of the dynamical model at the quadrupole-level approximation (which is an integral model), shown in the $(2h_2, H_2)$ space. The left panel is for $e_1 = 0.1$ and the right one is for $e_1 = 0.5$. The red lines correspond to the dynamical separatrices, which divide the whole phase space into regions of circulation and libration. Inside the region bounded by the separatrix, the ascending node of CBPs is of libration. It is referred to as nodal resonance in this paper. Under the quadrupole-level approximation, the conventional ZLK resonance for inner test particles is replaced by the nodal resonance for outer test particles (i.e., the libration of argument of pericentre ω_1 is replaced by the libration of longitude of ascending node Ω_2).

nian model in the cases of $e_1 = 0.1$ and $e_1 = 0.5$. It is observed that the nodal libration centre is located at $(2h_2 = \pi, H_2 = 0)$ and the saddle point is at $(2h_2 = 0, H_2 = 0)$. The dynamical separatrix, corresponding to the level curves of Hamiltonian passing through the saddle point, is shown in red lines. Dynamical separatrix can be found in Poincaré section shown in Fig. 5. Evidently, the separatrix plays a role in dividing the phase space into regions of nodal libration and circulation. The libration zone is surrounded by dynamical separatrix and the island of nodal libration is larger with a higher value of binary's eccentricity e_1 .

5.2 Orbit classifications

Under the quadrupole-order model, both the Hamiltonian \mathcal{H} and the planetary eccentricity e_2 are integral of motion. Here let us classify the motion in the space spanned by conserved parameters. It is similar to the well-known Lidov triangle in the (e_1, e_2) space (Lidov 1962; Shevchenko 2016). Similar discussions can be found in Lei & Huang (2022).

From the phase portraits shown in Fig. 6, it is observed that the saddle point is located at $(2h_2 = 0, H_2 = 0)$. According to the definition of dynamical separatrix, we can get the Hamiltonian of separatrix

$$\mathcal{H}_{\text{sep}} = -2(6e_1^2 - 1)(1 - e_2^2). \quad (20)$$

\mathcal{H}_{sep} is a decreasing function of e_2 if $e_1 < 1/\sqrt{6}$ and it is an increasing function of e_2 if $e_1 > 1/\sqrt{6}$. In particular, \mathcal{H}_{sep} is equal to zero when $e_1 = 1/\sqrt{6}$.

The minimum value of Hamiltonian takes place at $H_2 = G_2$ (i.e., $i_2 = 0^\circ$). Thus, the lower boundary of Hamiltonian can be expressed as

$$\mathcal{H}_{\text{lower}} = -(6e_1^2 + 4)(1 - e_2^2), \quad (21)$$

which is an increasing function of e_2 .

The maximum Hamiltonian happens at the libration centre $(2h_2 = \pi, H_2 = 0)$. As a result, the upper boundary

of Hamiltonian can be given by

$$\mathcal{H}_{\text{upper}} = (18e_1^2 + 2)(1 - e_2^2), \quad (22)$$

which is a decreasing function of e_2 .

Fig. 7 shows the distribution of librating and circulating orbits in the (e_2, \mathcal{H}) space for the cases of $e_1 = 0.1$ (see the left panel) and $e_1 = 0.5$ (see the right panel). The lower boundary, separatrix and the upper boundary are marked by black line, red line and blue line, respectively. Centres of nodal libration occupy on the upper boundary. The green shaded regions bounded by the separatrix and the lower boundary are of nodal circulation, the blue shaded regions bounded by the separatrix and upper boundary are of nodal libration, and the white zones (below the lower boundary or above the upper boundary) stand for the physically forbidden regions. It is observed that the area of nodal libration region increases with the binary's eccentricity e_1 . For a given e_1 , the range of Hamiltonian decreases with planetary eccentricity e_2 .

5.3 Width of nodal resonance

According to equation (20), we can get the expression of separatrix in the form of e_1 , i_2 and h_2 as follows:

$$(2 + 3e_1^2) \cos^2 i_2 + 5e_1^2 (\sin^2 i_2 \cos 2h_2 - 1) = 0 \quad (23)$$

For a given h_2 , there are two values of i_2 (see the phase portraits shown in Fig. 6). Usually, resonant width is used to measure the size of libration island, which takes the maximum when it is evaluated at the libration centre (i.e., $2h_2 = \pi$). Taking $2h_2 = \pi$ in equation (23), we can get

$$(1 + 4e_1^2) \cos^2 i_{2,\text{sep}} - 5e_1^2 = 0$$

which leads to

$$\cos i_{2,\text{sep}} = \pm \sqrt{\frac{5e_1^2}{1 + 4e_1^2}}.$$

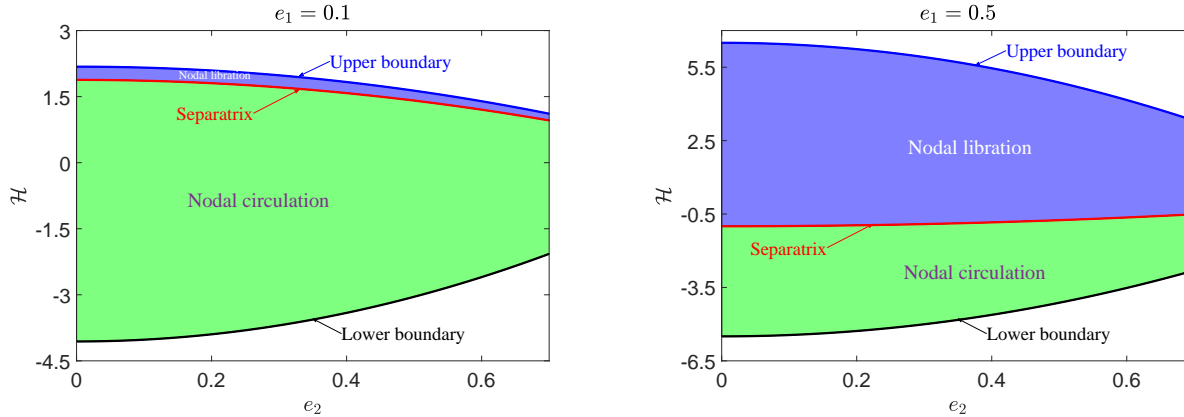


Figure 7. Distribution of the nodal libration and circulation regions in the (e_2, \mathcal{H}) space. The left panel is for $e_1 = 0.1$ and the right panel is for $e_1 = 0.5$. In both panels, dynamical separatrix between the libration and circulation regions is marked by red line. The white space represents the physically forbidden region.

It shows that the inclinations of the lower and upper separatrices at $2h_2 = \pi$ are

$$i_{2,\text{low}} = \arccos\left(\sqrt{\frac{5e_1^2}{1+4e_1^2}}\right),$$

$$i_{2,\text{up}} = \pi - \arccos\left(\sqrt{\frac{5e_1^2}{1+4e_1^2}}\right),$$

which are consistent with the critical inclinations for alternation between nodal libration and circulation (Doolin & Blundell 2011; Farago & Laskar 2010; Li et al. 2014; Chen et al. 2019; Martin & Lubow 2019). It means that the critical inclinations $i_{2,\text{low}}$ and $i_{2,\text{up}}$ are symmetric with respect to 90° . As a result, the resonant width, denoted by Δi_2 , can be obtained by

$$\Delta i_2 = i_{2,\text{up}} - i_{2,\text{low}} = \pi - 2 \arccos\left(\sqrt{\frac{5e_1^2}{1+4e_1^2}}\right) \quad (24)$$

which shows that the resonant width is only related to binary's eccentricity e_1 and it is an increasing function of e_1 .

Fig. 8 shows distribution of nodal libration and circulation regions in the (i_2, e_2) space for the case of $e_1 = 0.5$ (see the left panel) and in the (e_1, i_2) space for arbitrary binary's eccentricities (see the right panel). It is observed that the resonant width Δi_2 is independent on e_2 (see the left panel) and it is an increasing function of e_1 (see the right panel), which is in agreement with the prediction of equation (24). In particular, when the binary moves on a circular orbit ($e_1 = 0$), the nodal resonance disappears because of $\Delta i_2 = 0$ in this case.

It is interesting to note that the distribution of libration and circulation regions in the (i_2, e_2) space (see the left panel of Fig. 8) is similar to that of the conventional ZLK resonance of the inner test particles in the (i_1, e_1) space (Lei 2021). However, the dynamics is different. For the case of inner test particles, the resonant argument is $2\omega_1$ (ZLK oscillations), the location of separatrix in the (i_1, e_1) space is fixed at 39.8° and 140.2° and the motion integral is the z -component of particle's angular momentum $H = \sqrt{1 - e_1^2} \cos i_1$ (Lidov 1962; Kozai 1962). For the case

of outer test particles (the topic in this work), the resonant argument is $2\Omega_2$ (nodal oscillation), the location of separatrix in the (i_2, e_2) space is dependent on binary's eccentricity e_1 and the motion integral is the test particle's eccentricity e_2 (Naoz et al. 2017).

To conclude, we can see that the dynamics of quadrupole-order model is determined by two parameters: the binary eccentricity e_1 and planetary inclination i_2 . This is the reason that we discuss dynamical structures in the (i_2, e_1) space in this work.

5.4 Web of resonances

Considering the quadrupole-order Hamiltonian model is integrable, we could introduce Arnold action-angle variables (Morbiddelli 2002)

$$g_2^* = g_2 - \rho_g(t, G_2^*, H_2^*) = g_2^*(0) + \frac{2\pi}{T_g} t,$$

$$G_2^* = G_2,$$

$$h_2^* = h_2 - \rho_h(t, G_2^*, H_2^*) = h_2^*(0) + \frac{2\pi}{T_h} t, \quad (25)$$

$$H_2^* = \frac{1}{2\pi} \oint H_2 dh_2$$

which is a canonical transformation with the generating function,

$$\mathcal{S}(g_2, h_2, G_2^*, H_2^*) = h_2 H_2^* + \int H_2 dh_2$$

leading to the mutual transformation

$$G_2 = \frac{\partial \mathcal{S}}{\partial g_2}, \quad g_2^* = \frac{\partial \mathcal{S}}{\partial G_2^*} = \frac{\partial}{\partial G_2^*} \int H_2 dh_2,$$

$$H_2 = \frac{\partial \mathcal{S}}{\partial h_2}, \quad h_2^* = \frac{\partial \mathcal{S}}{\partial H_2^*} = h_2 + \frac{\partial}{\partial H_2^*} \int H_2 dh_2.$$

In the transformation given by equation (25), H_2^* is called Arnold action and it requires $h_2^*(0) = 0$. Without loss of generality, we assume that the state at the initial moment is $h_2(0) = \pi/2$ (it further requires $H_2(0) > 0$ for librating cycles). T_g and T_h are periods of g_2 and h_2 under the quadrupole-order Hamiltonian model. $\rho_g(t, G_2^*, H_2^*)$ and

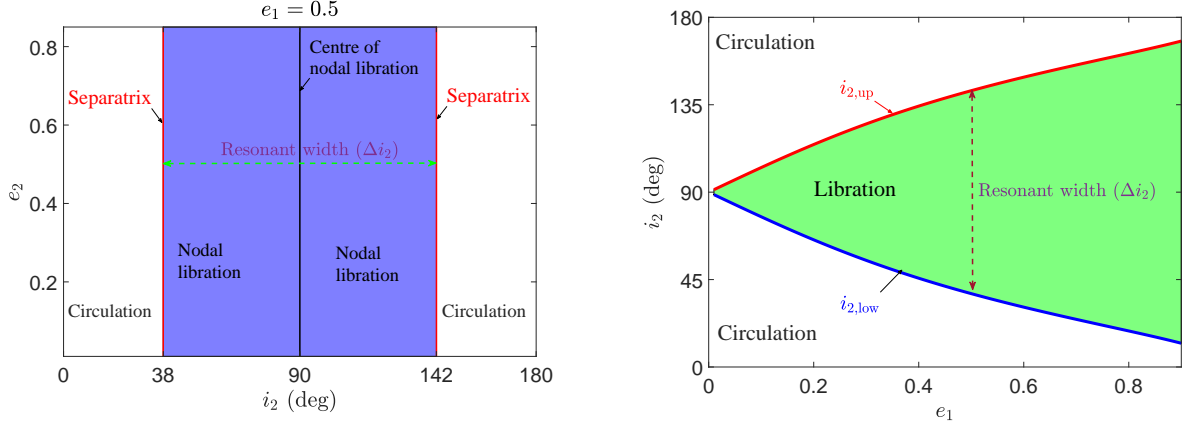


Figure 8. Distribution of nodal libration and circulation regions in the (i_2, e_2) space for the case of $e_1 = 0.5$ (left panel) and in the (e_1, i_2) space for arbitrary planetary eccentricities (right panel) with the longitude of ascending node at $2h_2 = \pi$ (libration centre). The shaded region is of libration and the white regions are of circulation. In both panels, the resonant width denoted by Δi_2 represents the distance of test particle's inclination between separatrices, evaluated at the libration centre. In the left panel, resonant width Δi_2 is plotted as a function of particle's eccentricity e_2 and in the right panel it is plotted as a function of the perturber's eccentricity e_1 (right panel). It is observed that the resonant width is independent on planetary eccentricity e_2 (see the left panel), while it is an increasing function of binary eccentricity e_1 (see the right panel).

$\rho_h(t, G_2^*, H_2^*)$ are periodic functions with zero average and have the same period of nodal cycle T_h (Henrard 1990). It requires that the initial angles $g_2(0)$ and $g_2^*(0)$ should be coincident, showing that $\rho_g(t=0) = \rho_g(t=T_h) = 0$.

In order to compute Arnold action H_2^* , we could integrate the following set of differential equation over one period of h_2 ,

$$\begin{cases} \dot{h}_2 = \frac{\partial \mathcal{H}}{\partial H_2}, \\ \dot{H}_2 = -\frac{\partial \mathcal{H}}{\partial h_2}, \\ \dot{H}_2^* = \frac{1}{2\pi} H_2 \frac{\partial \mathcal{H}}{\partial H_2}. \end{cases}$$

starting from the initial condition at $(h_{2,0} = \pi/2, H_{2,0}, H_{2,0}^* = 0)$.

Performing the following transformation

$$(g_2, h_2, G_2, H_2) \leftrightarrow (g_2^*, h_2^*, G_2^*, H_2^*)$$

it is possible to write the quadrupole-level Hamiltonian as

$$\mathcal{H}(h_2, G_2, H_2) \Rightarrow \mathcal{H}(G_2^*, H_2^*). \quad (26)$$

The Hamiltonian, which is independent on action variables, is referred to as the normal form. Under the set of action-angle variables, the angles (g_2^*, h_2^*) are cyclic variables, showing that the action variables (G_2^*, H_2^*) are motion integral. As a result, (g_2^*, h_2^*) are linear functions of time with fundamental frequencies of $2\pi/T_g$ and $2\pi/T_h$ (see equation 25). Please refer to Fig. 9 for the relationship between (g_2, h_2) and (g_2^*, h_2^*) for the circulating cycle (see the left panel) and the librating cycle (see the right panel). As expected, the original angles are nonlinear functions of time, while the variables after transformation are linear functions of time.

Applying the normal form of Hamiltonian to the canonical relation yields the fundamental frequencies as follows:

$$\begin{aligned} \dot{g}_2^* &= \frac{\partial \mathcal{H}}{\partial G_2^*}, \\ \dot{h}_2^* &= \frac{\partial \mathcal{H}}{\partial H_2^*}. \end{aligned} \quad (27)$$

The fundamental frequencies determines the nominal location of resonances,

$$k_1 \dot{h}_2^* + k_2 \dot{g}_2^* = 0 \quad (28)$$

where $k_1 \in \mathbb{N}$ and $k_2 \in \mathbb{Z}$.

Fig. 10 presents the resonance curves with $|k_2| = 1$ and $k_1 = \{0, 1, 2, 3\}$ in the (i_2, e_1) space. The shaded zone stands for the nodal libration region, which is the same as the right panel of Fig. 8. Inside the nodal libration region, secular resonances between g_2^* and h_2^* are referred to as secondary resonances and the ones outside the nodal libration region are called high-order resonances. In particular, the resonance with $k_1 = 0$ is the so-called inverse ZLK resonance with $\sigma = \omega_2$ as the resonant argument (de Elia et al. 2019; Vinson & Chiang 2018). According to the Hamiltonian given by equation (3), we can see that the inverse ZLK resonance is of hexadecapolar order. In particular, when the binary's eccentricity is zero, we can see that the inclinations of inverse ZLK resonance are equal to $i_2 = 63.4^\circ$ and $i_2 = 116.6^\circ$, which is consistent with the critical inclinations derived by Gallardo et al. (2012) and de Elia et al. (2019).

It should be noted that the distribution of resonant curves shown here is representative because it is independent on the eccentricity of particles e_2 , the mass parameter of the inner binary μ_b and semimajor axis ratio $\alpha = a_1/a_2$. Black crosses represent the location of observed CBPs with the semimajor axis ratio smaller than 1/3. See Table 1 for their detailed parameters. We can see that all the observed CBPs are in nearly co-planar configurations, and thus they are weakly influenced by high-order and/or secondary resonances.

From Fig. 10, we could know the nominal location of

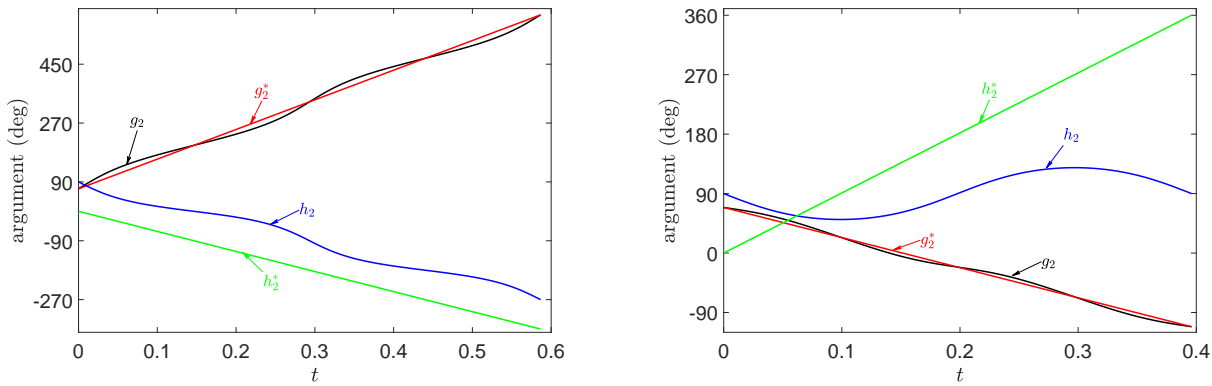


Figure 9. Relationship between the original variables g_2 and h_2 as well as the associated transformed variables g_2^* and h_2^* for the nodal circulating case (left panel) and for the nodal librating case (right panel).

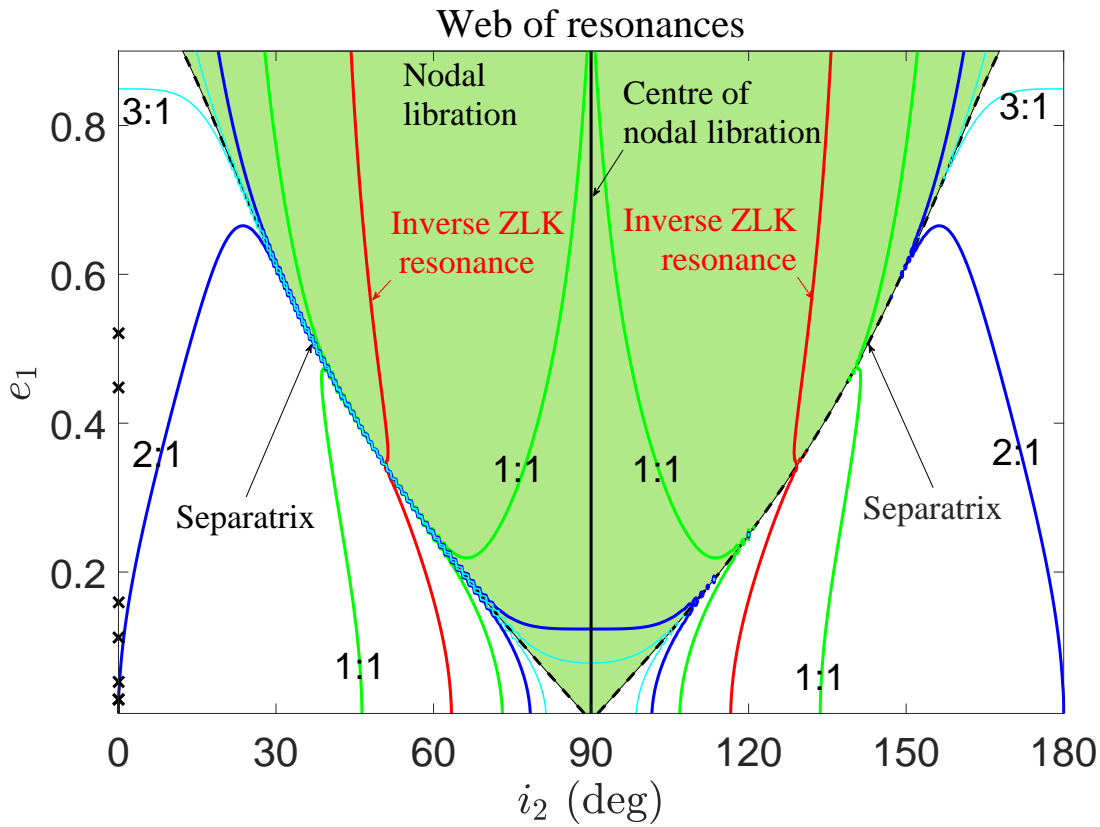


Figure 10. Web of resonances, standing for the distribution of nominal location of high-order and secondary resonances shown in the (i_2, e_1) space. The shaded region represents the parameter space where the nodal resonance takes place (it is similar to the right panel of Fig. 8) and the white regions are of nodal circulation. Secondary resonances happen inside the region of nodal resonance and high-order resonances takes place outside the region of nodal resonance. The red lines stand for the inverse ZLK resonance. Black crosses represent the location of observed CBPs (see Table 1 for their detailed parameters).

resonances. However, there is no resonant strength under the quadrupole-level approximation. Only if the octupole-order and hexadecapolar-order terms are included, the associated curves of high-order or secondary resonances may be replaced by a certain zone of libration around the nominal curve of resonance and the area of libration zone is proportional to the resonance strength. As expected, for the unequal-mass binary, the octupole-order resonances would have higher strength and the hexadecapolar-order resonances would hold weaker strength. However, it is different for the equal-mass case where all the resonances are of hexadecapolar order because of disappearance of octupole-order Hamiltonian, thus it is expected that all of them have comparable strength. This is in agreement with the dynamical maps shown in Fig. 4.

6 APPLICATIONS TO NUMERICAL STRUCTURES

In this section, resonance curves associated with high-order and secondary resonances between g_2^* and h_2^* discussed in the previous section are utilised to explain dynamical structures produced under the hexadecapolar-order Hamiltonian model.

6.1 Nodal and Inverse ZLK resonances

The nodal resonance with argument of $\sigma = 2\Omega_2$ is of quadrupole order and, without doubt, it dominates the main structure. The inverse ZLK resonance has been studied in [Vinson & Chiang \(2018\)](#) and [de Elia et al. \(2019\)](#) under the hexadecapolar-level approximation. The resonant argument is $\sigma = \omega_2$ and its strength is of hexadecapolar order. It is much weaker than the conventional ZLK resonance which is of quadrupole order in strength ([Lidov 1962](#); [Kozai 1962](#)).

Here we numerically explore dynamical structures caused by nodal resonance and inverse ZLK resonance. To produce the numerical structures, the initial angles are assumed at $g_{2,0} = \pi/2$ and $h_{2,0} = \pi/2$ and the secular equations of motion at the hexadecapolar-level approximation are numerically integrated over 10 nodal periods. The points with libration of h_2 and/or g_2 are recorded. Numerical structures are shown in Fig. 11. In practical simulations, $m_1 = 0.5m_\odot$ is taken for the unequal-mass case, and $m_1 = 1.0m_\odot$ is taken for the equal-mass case.

In Fig. 11, black dots stand for nodal resonance and blue dots represent the inverse ZLK resonance. For comparison, the nominal location of inverse ZLK resonance and dynamical separatrix of nodal resonance are also plotted. See the green dashed lines for dynamical separatrix and the solid red lines for nominal location of inverse ZLK resonance. It is observed that (a) there are qualitatively similar numerical structures caused by nodal resonance and inverse ZLK resonance with different parameters of μ_b , (b) numerical structures are nearly symmetric with respect to $i_2 = 90^\circ$, meaning that nodal and inverse ZLK resonances will not lead to symmetry breaking, (c) the distribution of nodal resonance in the (i_2, e_1) space presents the V-shape structure bounded by the dynamical separatrix of nodal resonance, which is dominated by the quadrupole-order dynamics discussed in

the previous section, (d) the inverse ZLK resonance can happen in almost the entire e_1 space, which is in agreement with the discussion given by [de Elia et al. \(2019\)](#), (e) for a given e_1 the libration zone of inverse ZLK resonance is very narrow because it is of hexadecapolar order, (f) the inverse ZLK resonance happens outside the nodal libration region if the binary's eccentricity e_1 is smaller than ~ 0.35 , else it happens inside the nodal libration region, and (g) excellent agreement can be observed between the analytical and numerical results for the structures.

6.2 Dynamical structures

Dynamical maps corresponding to $m_1 = 0.5m_\odot$ (standing for unequal-mass configuration) and $m_1 = 1.0m_\odot$ (standing for equal-mass configuration) together with web of resonances are shown in Fig. 12. For convenience, dynamical separatrix of nodal resonance is marked by black dashed lines, which form the main V-shape structure in the (i_2, e_1) space.

Fig. 12 shows that there is a perfect correspondence between dynamical structures and resonance curves. It is observed that (a) the main V-shape structure is dominated by the nodal resonance which is of quadrupole order in strength, (b) the structures inside the nodal libration region are governed by secondary resonances, and (c) the structures outside the nodal libration region are dominated by high-order secular resonances. In the unequal-mass case, the 1:1 resonance is of octupole order and the remaining resonances are of hexadecapolar order. In the equal-mass case, all the high-order and secondary resonances are of hexadecapolar order.

As shown in Table 1, CBPs currently detected so far are almost co-planar to the binary orbit. This is due to the fact that misaligned CBPs are more difficult to detect. However, in recent years polar-aligned circumbinary gas disk (HD 98800 B) and debris disk (99 Herculis) have been observed around eccentric binaries ([Kennedy et al. 2019, 2012](#); [Smallwood et al. 2020](#)), indicating that it is possible for formation of polar planets. In addition, it is more likely to form CBPs on polar orbits than on co-planar orbits, predicting that polar-aligned terrestrial planets may be found in the future ([Childs & Martin 2021](#)). In the polar region, an unexpected symmetry breaking is found between prograde and retrograde configurations around eccentric binary ([Cuello & Giuppone 2019](#)).

If we focus on the structures inside the polar region, we can further find from Fig. 12 that the dynamics is dominated by the nodal resonance when $e_1 < 0.22$ and it is governed by the nodal resonance in combination with the secondary 1:1 resonance when $e_1 > 0.22$. In addition, we can observe that the culprit causing symmetry breaking of dynamical structures inside polar region is the secondary 1:1 resonance.

7 SECONDARY RESONANCES

It is observed from Fig. 5 that (a) in the configuration of $e_1 = 0.1$ there are islands of libration associated with high-order resonances (including 1:1, 2:1 and 3:1 resonances located outside the nodal libration region) as well as secondary 3:1 resonance (inside the nodal libration region) and (b) in

Table 1. Parameters of CBPs shown in Fig. 10, where the semimajor axis ratio is smaller than $1/3$. Here i_2 is the relative inclination of planets with respect to the orbit of the inner binary.

System	$m_1(m_\odot)$	$m_2(m_\odot)$	$m_2(m_J)$	$i_2(^{\circ})$	$a_1(\text{au})$	$a_2(\text{au})$	e_1	e_2	Ref.
Kepler-34	1.0479	1.0208	0.22	1.81	0.22882	1.0896	0.52087	0.182	Welsh et al. (2012)
Kepler-47 (c)	0.957	0.342	0.05984	1.165	0.08145	0.6992	0.0288	0.024	Orosz et al. (2012)
Kepler-47 (d)	0.957	0.342	0.00997	1.38	0.08145	0.9638	0.0288	0.044	Orosz et al. (2019)
Kepler-453	0.944	0.1951	0.05	2.258	0.18539	0.7903	0.0524	0.0359	Welsh et al. (2015)
Kepler-1647	1.21	0.975	1.52	2.9855	0.1276	2.7205	0.1593	0.0581	Kostov et al. (2016)
Kepler-1661	0.841	0.262	0.053	0.93	0.187	0.633	0.112	0.057	Socia et al. (2020)
TIC 172900988	1.2388	1.2023	2.74	1.45	0.191928	0.89809	0.44793	0.088	Kostov et al. (2021)

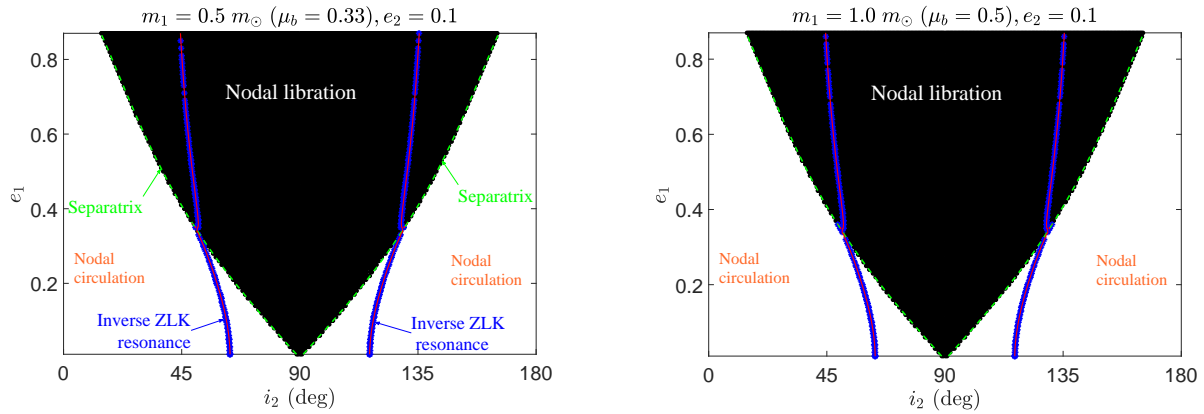


Figure 11. Numerical distribution of the nodal resonance (black dots) and inverse ZLK resonance (blue dots), determined under the hexadecapolar-order dynamical model. The left panel is for $m_1 = 0.5m_\odot$ representing the case of unequal-mass binary and the right panel is for $m_1 = 1.0m_\odot$ representing the case of equal-mass binary. The red lines stand for the nominal location of inverse ZLK resonance (similar to Fig. 6), and the green dashed lines stand for the dynamical separatrices of nodal resonance.

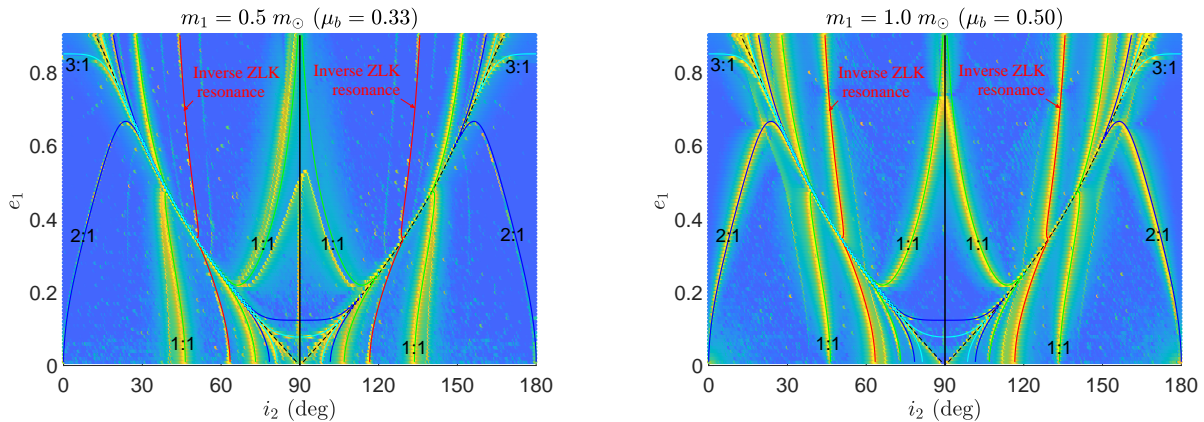


Figure 12. The nominal location of nodal resonance, high-order resonance as well as secondary resonances are plotted together with dynamical maps. The left panel is for the case of $m_1 = 0.5m_\odot$ and the right panel is for the case of $m_1 = 1.0m_\odot$. Excellent agreement can be observed between the numerical structures arising in dynamical maps and resonance curves determined under the quadrupole-level approximation.

the configuration of $e_1 = 0.3$ all the motion happen inside the nodal libration region and there are two islands of libration, corresponding to the 1:1 bifurcation. In this section, we will analytically study secondary resonances inside the nodal libration zone by means of perturbative treatments.

7.1 Perturbative treatment

Under the set of action-angle variables $(g_2^*, h_2^*, G_2^*, H_2^*)$ defined by equation (25), the hexadecapolar-order Hamiltonian can be expressed as

$$\mathcal{H}(g_2^*, h_2^*, G_2^*, H_2^*) = \mathcal{H}_0(G_2^*, H_2^*) + \varepsilon \mathcal{H}_1(g_2^*, h_2^*, G_2^*, H_2^*) \quad (29)$$

which is composed of the unperturbed Hamiltonian $\mathcal{H}_0(G_2^*, H_2^*)$ corresponding to the quadrupole-order component and the perturbation Hamiltonian $\mathcal{H}_1(g_2^*, h_2^*, G_2^*, H_2^*)$ corresponding to the octupole- and hexadecapolar-order components. In general, the perturbation part is much smaller than the unperturbed term, showing that such a Hamiltonian model can be treated by means of perturbation theory. In this section, we will take advantage of perturbation theories proposed by Wisdom (1985) and Henrard & Lemaître (1986) to study the resonant dynamics. It should be mentioned that similar approach of Henrard's method is adopted by Li et al. (2014) to study dynamics of low-inclination and nearly polar CBPs. In particular, excitation of planetary eccentricity in near coplanar configurations is analytically discussed in Moriwaki & Nakagawa (2004), Leung & Lee (2013) and Li et al. (2014).

According to Sect. 6, it is shown that the unperturbed Hamiltonian $\mathcal{H}_0(G_2^*, H_2^*)$ produces the fundamental frequencies and their integer commensurability determines the nominal location of resonances between g_2^* and h_2^* . To study the dynamics of $k_1:k_2$ resonance, it is convenient for us to introduce the following transformation,

$$\begin{aligned} \sigma_1 &= h_2^* + \frac{k_2}{k_1} g_2^*, & \Sigma_1 &= H_2^*, \\ \sigma_2 &= g_2^*, & \Sigma_2 &= G_2^* - \frac{k_2}{k_1} H_2^* \end{aligned} \quad (30)$$

which is canonical with the generating function

$$S(g_2^*, h_2^*, \Sigma_1, \Sigma_2) = h_2^* \Sigma_1 + g_2^* \left(\frac{k_2}{k_1} \Sigma_1 + \Sigma_2 \right).$$

In terms of the canonical variables $(\sigma_1, \sigma_2, \Sigma_1, \Sigma_2)$, the hexadecapolar-order Hamiltonian can be written as

$$\mathcal{H}(\sigma_1, \sigma_2, \Sigma_1, \Sigma_2) = \mathcal{H}_0(\Sigma_1, \Sigma_2) + \varepsilon \mathcal{H}_1(\sigma_1, \sigma_2, \Sigma_1, \Sigma_2). \quad (31)$$

When a circumbinary planet is located inside the $k_1:k_2$ resonance, it holds $k_1 h_2^* + k_2 g_2^* \approx 0$, meaning that $\dot{\sigma}_1 \approx 0$. As a result, the time derivatives of σ_1 and σ_2 satisfy the hierarchical relation $\dot{\sigma}_1 \ll \dot{\sigma}_2$, showing that equation (31) determines a separable Hamiltonian model (Henrard 1990). In particular, (σ_1, Σ_1) stands for the slow degree of freedom and (σ_2, Σ_2) stands for the fast degree of freedom. According to Wisdom's perturbation theory (Wisdom 1985), during the timescale of the fast degree of freedom (for example, one period of σ_2), the slow variables (σ_1, Σ_1) have negligible change and thus they can be approximated as parameters. Under the assumption with (σ_1, Σ_1) as parameters, equation (31)

reduces to an integrable Hamiltonian model with (σ_2, Σ_2) as phase-space variables. Regarding the integrable Hamiltonian, it is possible to introduce action-angle variables as follows (Morbidelli 2002):

$$\sigma_2^* = \frac{2\pi}{T} t, \quad \Sigma_2^* = \frac{1}{2\pi} \int_0^{2\pi} \Sigma_2 d\sigma_2 \quad (32)$$

where T is the period of σ_2 . Under the set of action-angle variables (σ_2^*, Σ_2^*) , the hexadecapolar-order Hamiltonian becomes

$$\mathcal{H}(\sigma_1, \Sigma_1, \Sigma_2^*) = \mathcal{H}_0(\Sigma_1, \Sigma_2^*) + \varepsilon \mathcal{H}_1(\sigma_1, \Sigma_1, \Sigma_2^*) \quad (33)$$

where σ_2^* is a cyclic variable, indicating that its conjugate momentum Σ_2^* is a motion integral, which remains constant during the long-term evolution. Such a motion integral Σ_2^* is usually referred to as the adiabatic invariant (Henrard 1990). For convenience, we denote the adiabatic invariant as

$$S = \Sigma_2^* = \frac{1}{2\pi} \int_0^{2\pi} \Sigma_2 d\sigma_2 \quad (34)$$

which measures the path integration of the phase curve in the (σ_2, Σ_2) space (divided by 2π).

For the two-degree-of-freedom model governed by the Hamiltonian (31), there are two conserved quantities during the long-term evolution: (a) the Hamiltonian \mathcal{H} itself and (b) the adiabatic invariant S . As a result, the dynamical model becomes approximately integrable.

7.2 Phase-space structures

Regarding the integrable two-degree-of-freedom Hamiltonian model, the phase-space structures can be explored by analysing phase portraits: (a) plotting level curves of the Hamiltonian \mathcal{H} under a given adiabatic invariant S or (b) plotting level curves of the adiabatic invariant S under a given Hamiltonian \mathcal{H} . Both versions of phase portraits are equivalent. The former definition of phase portraits is adopted in Saillenfest et al. (2016) and Saillenfest (2020), and the latter definition of phase portraits is taken in Lei (2022) and Lei et al. (2022).

For the current problem, the Hamiltonian \mathcal{H} is easy to calculate because it has an explicit expression, while the adiabatic invariant is relatively difficult to determine. Thus, in this work we produce phase portraits by plotting level curves of the adiabatic invariant S under a given Hamiltonian \mathcal{H} (i.e., the second definition). As mentioned in Sect. 4, the Hamiltonian is characterised by the critical inclination $i_{2,c}$.

Fig. 13 presents phase-space structures of the 1:1 secondary resonances under the configurations with $m_1 = 0.1m_\odot$, $e_1 = 0.3$ and $i_{2,c} = 61^\circ$, and Fig. 14 corresponds to the case of $m_1 = 0.5m_\odot$, $e_1 = 0.3$ and $i_{2,c} = 63^\circ$. Red lines stand for the dynamical separatrices, which play a role in dividing regions of libration and circulation associated with secondary resonance. For comparison, the associated Poincaré sections are provided in right panels. It is observed that (a) there is a perfect agreement between the analytical structures arising in phase portraits and numerical structures arising in Poincaré sections, (b) there are two islands

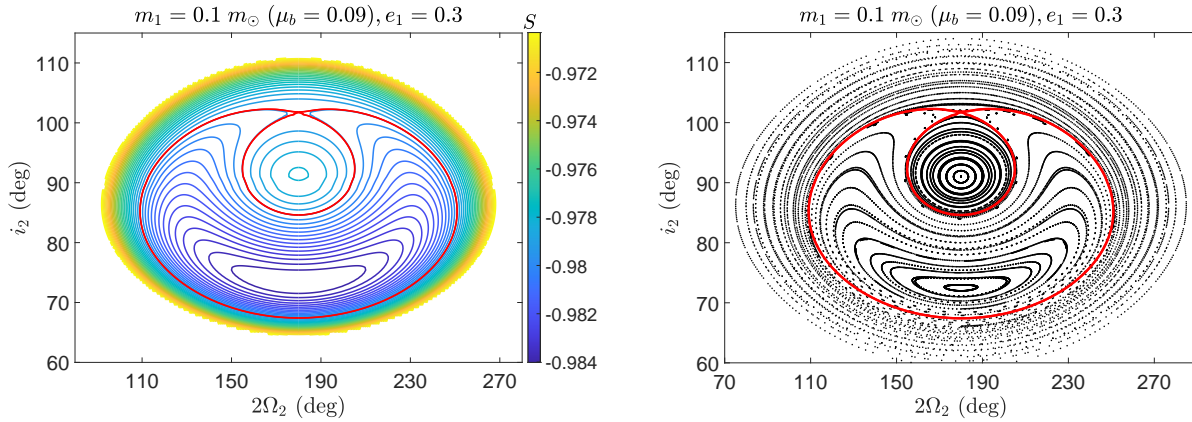


Figure 13. Dynamical structures of the 1:1 secondary resonances inside the nodal resonance (left panel), as well as the associated numerical structures arising in Poincaré sections (right panel) for CBPs with system parameters of $m_1 = 0.1 m_\odot$, $e_1 = 0.3$ and $i_{2,c} = 61^\circ$. The index shown in the colour bar represents the magnitude of the motion integral S . In both panels, red line stands for the dynamical separatrix arising in phase portrait. There is an excellent agreement between the analytical and numerical structures.

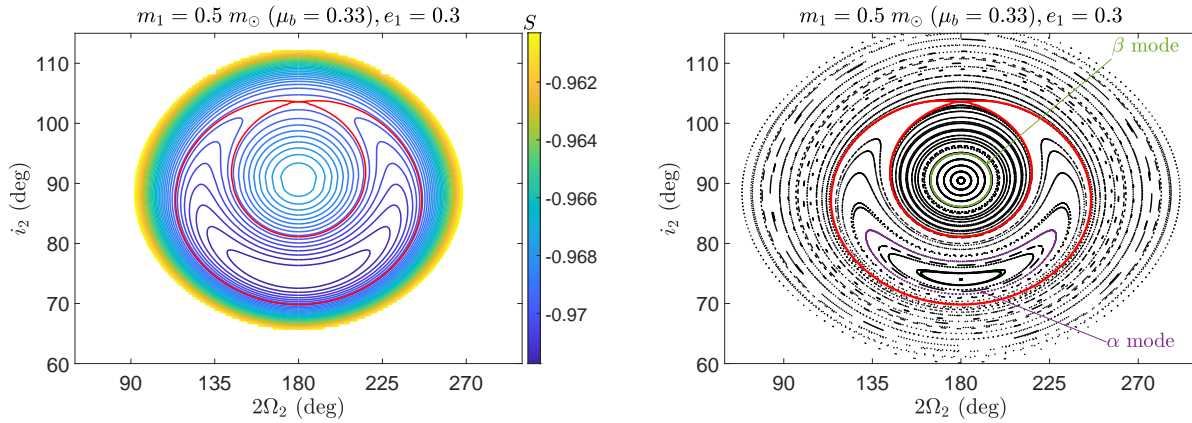


Figure 14. Similar to Fig. 13 but for the parameters of $m_1 = 0.5 m_\odot$, $e_1 = 0.3$ and $i_{2,c} = 63^\circ$. In the right panel, the bottom island of libration is denoted as α mode and the upper island of libration is denoted by β mode.

of libration, which are separated by the dynamical separatrix, and (c) the 1:1 secondary resonance is indeed the culprit that leads to symmetry breaking of dynamical structures.

In the Poincaré section, there are two islands of libration associated with 1:1 secondary resonance. For convenience, we denote the bottom island of libration as α mode and the upper island of libration as β mode. Please see the right panel of Fig. 14. In α and β modes, we take a representative trajectory in each mode as an example and show its time evolution of resonant arguments including $\sigma = h_2$ (for nodal resonance) and $\sigma = h_2^* + g_2^*$ (for secondary resonance) in Fig. 15. It is observed that (a) for the trajectory in α mode both the arguments $\sigma = h_2$ and $\sigma = h_2^* + g_2^*$ are of libration and (b) for the trajectory in β mode the argument of $\sigma = h_2$ is of libration while the argument of $\sigma = h_2^* + g_2^*$ is of circulation. Thus, secondary 1:1 resonance happens inside the α -mode island of libration.

It should be mentioned that although the simulations are performed for the secondary 1:1 resonance, which is the strongest among secondary resonances, the perturba-

tion method adopted in this work is applicable for other resonances shown in Fig. 10.

8 CONCLUSIONS

In this work, secular dynamics of CBPs is systematically investigated under the hierarchical three-body configuration, where the semimajor axis ratio $\alpha = a_1/a_2$ is a small parameter. The phase-averaged Hamiltonian truncated up to hexadecapolar order in α is derived and it is in agreement with the Hamiltonian form given in Naoz et al. (2017), Vinson & Chiang (2018) and de Elia et al. (2019). Numerical simulations show that the secular approximation at the hexadecapolar level could catch the long-term behaviours of orbit elements.

Initially, different versions of stability criteria are briefly introduced and compared for P-type configurations. The stability criteria given by Dvorak et al. (1989), Holman & Wiegert (1999) and Quarles et al. (2018) are suitable for low-inclination, low-eccentricity planetary orbits, the one

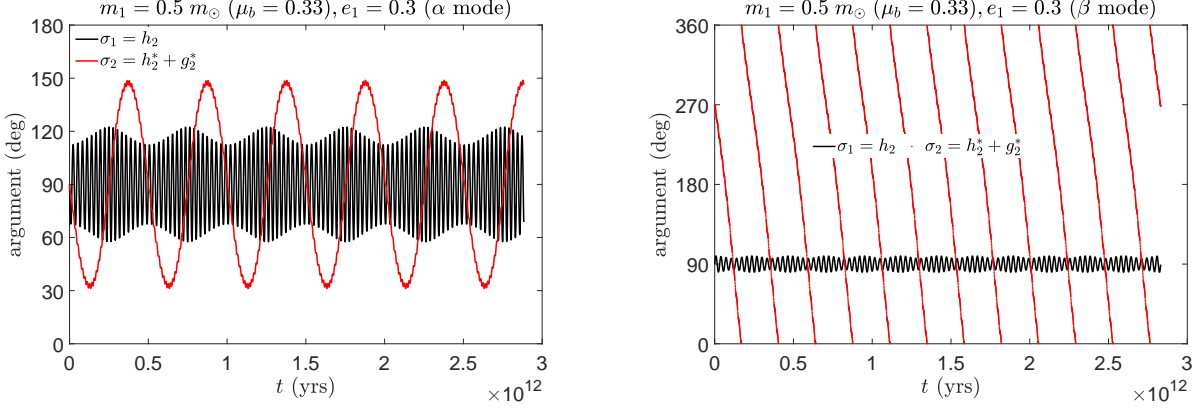


Figure 15. Time histories of the arguments associated with the nodal resonance $\sigma = h_2$ (black lines) and the secondary resonance $\sigma = h_2^* + g_2^*$ (red lines) for the trajectories marked in the right panel of Fig. 14. The left panel is for the α model and the right panel is for the β mode. Trajectories in both modes are inside the nodal resonance (i.e., Ω_2 of both trajectories is of libration). The initial condition of the trajectory in α mode is $e_{2,0} = 0.363$, $i_{2,0} = 77^\circ$ and $\Omega_{2,0} = \omega_{2,0} = \pi/2$, and the initial condition of the trajectory in β mode is $e_{2,0} = 0.278$, $i_{2,0} = 95^\circ$ and $\Omega_{2,0} = \omega_{2,0} = \pi/2$.

presented by Adelbert et al. (2023) is suitable for low-inclination planetary orbits with arbitrary eccentricities, and the ones developed in Mardling & Aarseth (2001) and Geor-gakarakos et al. (2024) can apply to inclined and eccentric planetary orbits. With a certain set of parameter, there exists different degrees of difference among the stability curves. In practice, we adopt the stability condition given by Mardling & Aarseth (2001) as a criterion to stop numerical integration.

Then, global structures of CBPs in the phase space are revealed by analysing dynamical maps, with the second-derivative-based indicator $||\Delta D||$ as index (see Fig. 4). It is found that structures arising in dynamical maps are weakly related to the mass parameter μ_b , semimajor axis ratio $\alpha = a_1/a_2$, planetary eccentricity e_2 . In the (i_2, e_1) space, there is a main V-shape structure and inside or outside the V-shape region there are complex minute structures. Dynamical maps could provide us a powerful tool to predict possible regions where the inner binary could host planets from the viewpoint of long-term stability. In the case of unequal-mass binary, significant symmetry breaking of dynamical structures is observed inside the polar region. However, the symmetry breaking is relatively weak for the case of equal-mass binary, because in this case the octupole-order contribution disappears. Furthermore, Poincaré surfaces of sections indicate that these dynamical structures are caused by nodal resonance, high-order and secondary resonances.

To understand the structures arising in dynamical maps and Poincaré sections, the dynamics under the quadrupole-order Hamiltonian is systematically explored. The quadrupole-level Hamiltonian determines an integrable model, where the phase-space structures can be revealed by plotting phase portraits. For convenience, we refer the quadrupole-order resonance as the nodal resonance with argument of $\sigma = 2\Omega_2$. It is found that the island of nodal libration increases with binary eccentricity e_1 . Orbit classifications are made in the (\mathcal{H}, e_2) space, where \mathcal{H} and e_2 are motion integral for the quadrupole-order Hamiltonian model. Expression of resonant width, denoted by Δi_2 , is

explicitly provided and it is only related to the binary eccentricity e_1 (an increasing function of e_1).

At the quadrupole-level approximation, the dynamics is distinctively different for inner and outer test particles. In particular, the quadrupole-order dynamics is determined by the binary eccentricity for the case of outer test particles, while it is independent on binary's eccentricity for the case of inner test particles (this observation is evident from their respective expression of quadrupole-level Hamiltonian). For the case of inner test particles, the quadrupole-order resonance is the conventional ZLK resonance with argument of $\sigma = 2\omega_1$ librating around π , the motion integral is the z -component of angular momentum $H = \sqrt{1 - e_1^2} \cos i_1$, and boundaries of inclination where the quadrupole-order resonance happens are 39.2° and 140.8° (Kozai 1962; Lidov 1962). When ZLK resonance takes place, it is possible to stimulate large oscillations in eccentricity and inclination, conserving the motion integral H . For the case of outer test particles, the quadrupole-order resonance is the nodal resonance with argument of $\sigma = 2\Omega_2$ librating around π , the motion integral is planetary eccentricity e_2 , and the boundaries of inclination where the quadrupole-order resonance takes place are dependent on the binary's eccentricity e_1 (see Fig. 8). The dynamical response is to excite planetary inclination by conserving the motion integral e_2 (planetary eccentricity remains unchanged), which is distinctively different from the case of inner test particles.

Regarding the integrable dynamical model determined by the quadrupole-order Hamiltonian, a canonical transformation is performed to introduce the set of action-angle variables. The quadrupole-level Hamiltonian can be expressed in a normal form, which determines the fundamental frequencies $(\dot{g}_2^*, \dot{h}_2^*)$. Consequently, a web of resonance, satisfying the relation $k_1 \dot{h}_2^* + k_2 \dot{g}_2^* = 0$, can be produced (see Fig. 10 for those dominant resonances). The curves of quadrupole-order resonance (nodal resonance), high-order resonances and secondary resonances are very important because they constitute the backbone dominating varieties of dynamical structures in phase space. It is observed that the CBPs detected

so far (see Table 1) are located in almost co-planar configurations and thus they are not influenced by the resonances. Resonance curves determined under the quadrupole-order Hamiltonian can well explain numerical structures (see Figs. 11 and 12). It is concluded that (a) the main V-shape structure is dominated by the quadrupole-order resonance (nodal resonance), (b) the dynamical structures inside the nodal libration region are governed by secondary resonances (as well as inverse ZLK resonance), (c) those structures outside the nodal libration region are sculpted by high-order resonances and (d) the secondary 1:1 resonance is the culprit that leads to symmetry breaking of dynamical structures inside polar region.

At last, perturbative treatments developed by Wisdom (1985) and Henrard & Lemaître (1986) are adopted to study secondary resonances. In particular, a set of action-angle variables is introduced by means of canonical transformation. When the circumbinary planet is located inside a certain secondary resonance, the hexadecapolar-order Hamiltonian determines a separable dynamical model, where the frequencies are hierarchical in magnitude. According to Wisdom's theory (Wisdom 1985), an adiabatic invariant (denoted by S) measuring the area bounded by the phase trajectory of the fast degree of freedom can be introduced. The conservation of Hamiltonian \mathcal{H} and adiabatic invariant S makes the current two-degree-of-freedom dynamical model be integrable. The dynamical structures can be explored by analysing phase portraits, corresponding to level curves of adiabatic invariant S with a given Hamiltonian \mathcal{H} . The secondary 1:1 resonance, which is the strongest one among secondary resonances, is taken as an example. Results show that (a) there is an excellent agreement between analytical structures arising in phase portraits and numerical structures arising in Poincaré sections, (b) the secondary 1:1 resonance corresponds to the bifurcation of the nodal resonance, and (c) the secondary 1:1 resonance is indeed the culprit causing symmetry breaking (with respect to $i_2 = 90^\circ$) of dynamical structures.

The results of this work provide a global picture about the dynamics of CBPs in a large range of parameters. In addition, our solutions in this work have potential applications to asteroids in Kuiper belt, debris discs around binary stars, circumbinary planets, and stars around binary supermassive black holes.

ACKNOWLEDGEMENTS

We wish to thank an anonymous referee for providing us helpful comments that improved the quality of the manuscript. This work is financially supported by the National Natural Science Foundation of China (Nos. 12073011, 12073019 and 12233003) and the National Key R&D Program of China (No. 2019YFA0706601).

DATA AVAILABILITY

The analysis and codes are available upon request.

REFERENCES

- Adelbert S., Penzlin A. B., Schäfer C. M., Kley W., Quarles B., Sfair R., 2023, *A&A*, 680, A29
- Borkovits T., Hajdu T., Sztakovics J., Rappaport S., Levine A., Bíró I. B., Klagyivik P., 2016, *MNRAS*, 455, 4136
- Brinch C., Jørgensen J. K., Hogerheijde M. R., Nelson R. P., Gressel O., 2016, *ApJL*, 830, L16
- Cazzoletti P., Ricci L., Birnstiel T., Lodato G., 2017, *A&A*, 599, A102
- Chen C., Franchini A., Lubow S. H., Martin R. G., 2019, *MNRAS*, 490, 5634
- Chen C., Lubow S. H., Martin R. G., 2020, *MNRAS*, 494, 4645
- Childs A. C., Martin R. G., 2021, *ApJL*, 920, L8
- Childs A. C., Martin R. G., 2022, *ApJL*, 927, L7
- Cuello N., Giuppone C. A., 2019, *A&A*, 628, A119
- Czekala I., Chiang E., Andrews S. M., Jensen E. L., Torres G., Wilner D. J., Stassun K. G., Macintosh B., 2019, *ApJ*, 883, 22
- Daquin J., Charalambous C., 2023, *Celest. Mech. Dyn. Astron.*, 135, 31
- Daquin J., Pédenon-Orlanducci R., Agaoglou M., García-Sánchez G., Mancho A. M., 2022, *Physica D: Nonlinear Phenomena*, 442, 133520
- de Elia G. C., Zanardi M., Dugaro A., Naoz S., 2019, *A&A*, 627, A17
- Doolin S., Blundell K. M., 2011, *MNRAS*, 418, 2656
- Dvorak R., Froeschlé C., Froeschle C., 1989, *A&A*, 226, 335
- Farago F., Laskar J., 2010, *MNRAS*, 401, 1189
- Ford E. B., Kozinsky B., Rasio F. A., 2000, *ApJ*, 535, 385
- Gallardo T., Hugo G., Pais P., 2012, *Icarus*, 220, 392
- Georgakarakos N., Eggl S., Ali-Dip M., Dobbs-Dixon I., 2024, arXiv preprint arXiv:2404.13746
- Getley A., Carter B., King R., O'Toole S., 2017, *MNRAS*, 468, 2932
- Guzzo M., Lega E., Froeschlé C., 2002, *Physica D: Nonlinear Phenomena*, 163, 1
- Harrington R. S., 1968, *AJ*, 73, 190
- Harrington R. S., 1969, *Celest. Mech.*, 1, 200
- Henrard J., 1990, *Celest. Mech. Dyn. Astron.*, 49, 43
- Henrard J., Lemaître A., 1986, *Celest. Mech.*, 39, 213
- Holman M. J., Wiegert P. A., 1999, *AJ*, 117, 621
- Huang X., Lei H., 2024, *AJ*, 167, 234
- Katz B., Dong S., Malhotra R., 2011, *Physical Review Letters*, 107, 181101
- Kennedy G., Wyatt M., Sibthorpe B., Duchêne G., Kalas P., Matthews B., Greaves J., Su K., Fitzgerald M., 2012, *MNRAS*, 421, 2264
- Kennedy G. M., Matrà L., Facchini S., Milli J., Panić O., Price D., Wilner D. J., Wyatt M. C., Yelverton B. M., 2019, *Nature Astronomy*, 3, 230
- Kostov V. B., Orosz J. A., Feinstein A. D., Welsh W. F., Cukier W., Haghighipour N., Quarles B., Martin D. V., Montet B. T., Torres G., et al., 2020, *AJ*, 159, 253
- Kostov V. B., Orosz J. A., Welsh W. F., Doyle L. R., Fabrycky D. C., Haghighipour N., Quarles B., Short D. R., Cochran W. D., Endl M., et al., 2016, *ApJ*, 827, 86
- Kostov V. B., Powell B. P., Orosz J. A., Welsh W. F., Cochran W., Collins K. A., Endl M., Hellier C., Latham D. W., MacQueen P., et al., 2021, *AJ*, 162, 234

- Kozai Y., 1962, *AJ*, 67, 591
- Lei H., 2020, *Astrodyn*, 4, 57
- Lei H., 2021, *Celest. Mech. Dyn. Astron.*, 133, 40
- Lei H., 2022, *AJ*, 163, 214
- Lei H., 2024, *AJ*, 167, 121
- Lei H., Huang X., 2022, *MNRAS*, 515, 1086
- Lei H., Li J., Huang X., Li M., 2022, *AJ*, 164, 74
- Lei H., Ortore E., Circi C., 2022, *Astrodyn*, 6, 357
- Lepp S., Martin R. G., Childs A. C., 2022, *ApJL*, 929, L5
- Leung G. C., Lee M. H., 2013, *The Astrophysical Journal*, 763, 107
- Li D., Zhou J., Zhang H., 2014, *MNRAS*, 437, 3832
- Lidov M., 1962, *P&SS*, 9, 719
- Lithwick Y., Naoz S., 2011, *ApJ*, 742, 94
- Liu B., Muñoz D. J., Lai D., 2015, *MNRAS*, 447, 747
- Mardling R. A., Aarseth S. J., 2001, *MNRAS*, 321, 398
- Martin D. V., 2018, arXiv preprint arXiv:1802.08693
- Martin D. V., Triaud A. H., 2014, *A&A*, 570, A91
- Martin R. G., Lubow S. H., 2017, *ApJL*, 835, L28
- Martin R. G., Lubow S. H., 2019, *MNRAS*, 490, 1332
- Martin R. G., Lubow S. H., Vallet D., Anugu N., Gies D. R., 2023, *ApJL*, 957, L28
- Morbidelli A., 2002, *Modern celestial mechanics: aspects of solar system dynamics*. Taylor & Francis, London and New York
- Moriwaki K., Nakagawa Y., 2004, *The Astrophysical Journal*, 609, 1065
- Murray C. D., Dermott S. F., 1999, *Solar system dynamics*. Cambridge university press
- Naoz S., 2016, *ARA&A*, 54, 441
- Naoz S., Farr W. M., Lithwick Y., Rasio F. A., Teyssandier J., 2013, *MNRAS*, 431, 2155
- Naoz S., Li G., Zanardi M., De Elía G. C., Di Sisto R. P., 2017, *AJ*, 154, 18
- Orosz J. A., Welsh W. F., Carter J. A., Fabrycky D. C., Cochran W. D., Endl M., Ford E. B., Haghighipour N., MacQueen P. J., Mazeh T., et al., 2012, *Science*, 337, 1511
- Orosz J. A., Welsh W. F., Haghighipour N., Quarles B., Short D. R., Mills S. M., Satyal S., Torres G., Agol E., Fabrycky D. C., et al., 2019, *AJ*, 157, 174
- Quarles B., Satyal S., Kostov V., Kaib N., Haghighipour N., 2018, *ApJ*, 856, 150
- Saillenfest M., 2020, *Celest. Mech. Dyn. Astron.*, 132, 1
- Saillenfest M., Fouchard M., Tommei G., Valsecchi G. B., 2016, *Celest. Mech. Dyn. Astron.*, 126, 369
- Shevchenko I. I., 2016, *The Lidov-Kozai effect-applications in exoplanet research and dynamical astronomy*. Vol. 441, Springer
- Smallwood J. L., Franchini A., Chen C., Becerril E., Lubow S. H., Yang C.-C., Martin R. G., 2020, *MNRAS*, 494, 487
- Socia Q. J., Welsh W. F., Orosz J. A., Cochran W. D., Endl M., Quarles B., Short D. R., Torres G., Windmiller G., Yenawine M., 2020, *AJ*, 159, 94
- Sybilski P., Konacki M., Kozłowski S., 2010, *MNRAS*, 405, 657
- Tokovinin A., 1997, *Astronomy Letters*, 23, 727
- Verhoeff A., Min M., Pantin E., Waters L., Tielens A., Honda M., Fujiwara H., Bouwman J., Van Boekel R., Dougherty S., et al., 2011, *A&A*, 528, A91
- Vinson B. R., Chiang E., 2018, *MNRAS*, 474, 4855
- Welsh W. F., Orosz J. A., Carter J. A., Fabrycky D. C., Ford E. B., Lissauer J. J., Prša A., Quinn S. N., Ragozzine D., Short D. R., et al., 2012, *Nature*, 481, 475
- Welsh W. F., Orosz J. A., Short D. R., Cochran W. D., Endl M., Brugamyer E., Haghighipour N., Buchhave L. A., Doyle L. R., Fabrycky D. C., et al., 2015, *ApJ*, 809, 26
- Wisdom J., 1985, *Icarus*, 63, 272
- Zhang Z., Fabrycky D. C., 2019, *ApJ*, 879, 92

This paper has been typeset from a $\text{\TeX}/\text{\LaTeX}$ file prepared by the author.